A PDF-based hybrid prognostic cloud scheme for general circulation models

M. Watanabe[1], S. Emori[1, 2,3], M. Satoh[1,3] and H. Miura[3]

1: Center for Climate System Research, University of Tokyo
2: National Institute for Environmental Studies
3: Frontier Research Center for Global Change, JAMSTEC

Climate Dynamics
Submitted on May 12, 2008
Revised on September 16, 2008
Revised on October 8, 2008
Revised on October 22, 2008

Corresponding author:
Dr. Masahiro Watanabe
Center for Climate System Research, University of Tokyo
5-1-5 Kashiwanoha, Kashiwa, Chiba 277-8568, Japan
E-mail: hiro@ccsr.u-tokyo.ac.jp

ABSTRACT

A new cloud parameterization based on prognostic equations for the subgrid-scale fluctuations in temperature and total water content is introduced for global climate models. The proposed scheme, called hybrid prognostic cloud (HPC) parameterization, employs simple probability density functions (PDFs) to the horizontal subgrid-scale inhomogeneity, allowing them to vary in shape in response to small-scale processes such as cumulus detrainment and turbulent mixing. Simple tests indicate that the HPC scheme is highly favorable as compared to a diagnostic scheme in terms of the cloud fraction and cloud water content under either uniform or non-uniform forcing.

The relevance of the HPC scheme is investigated by implementing it in an atmospheric component model of the climate model MIROC with a coarse resolution of T42. A comparison of the short-term integrations between the T42 model and a global cloud resolving model (GCRM) reveals that the HPC scheme can reproduce, to a certain degree, the subgrid-scale variance and skewness of temperature and total water content simulated in the GCRM. It is also found that the HPC scheme significantly alters the climatological distributions in cloud cover, precipitation, and moisture, which are all improved from the model using a conventional diagnostic cloud scheme.

Key words: cloud, parameterization, GCM, prognostic scheme, subgrid-scale PDF

1. Introduction

The representation of non-convective clouds in general circulation models (GCMs) is one of the important tasks involved in the simulation of realistic climate as well as for understanding its sensitivity to changes in external forcing because of their vital role in the global radiative budget and hydrological cycle. If the model grid spacing is sufficiently fine, such as that in cloud resolving models (CRMs), a water cloud can be formed simply when the grid becomes saturated. However, the current GCMs with a horizontal resolution of *O*(100km) cannot employ such all-or-nothing method; therefore, we must consider a subgrid-scale distribution of the thermodynamic and water variables without solving the subgrid-scale motions. This is the baseline for the cloud parameterization in large-scale models, and the simulated cloud cover and cloud-radiative forcing considerably vary among GCMs depending upon the schemes employed to parameterize clouds and condensation substances (e.g., Zhang et al. 2005; Bony and Dufresne 2005).

Earlier studies have focused on the development of *diagnostic* cloud parameterization by using the statistical relationship between the cloud and the grid-mean variables. A pioneering scheme was introduced by Sommeria and Deardorff (1977) and Mellor (1977), who assumed a joint probability density function (PDF) for the subgrid-scale liquid temperature and total water content, from which the cloud fraction and condensates were evaluated by integrating over the saturated part of the grid box. This concept of PDF-based parameterization, which is based on two assumptions that saturated air masses produce condensates immediately ("fast condensation assumption") and that the subgrid-scale distribution can be represented by a single PDF, yielded a number of variants for different PDFs (Bougeault 1981, 1982; Smith 1990; LeTreut and Li 1991; Ricard and Royer 1993; Lewellen and Yoh 1993; Lohmann et al. 1999, among others); these variants are collectively referred to as the statistical scheme. Another type of diagnostic scheme called the

relative humidity (RH) scheme relates the cloud production to the grid-mean RH (Sundqvist 1978; Slingo 1987; Xu and Randall 1996). Although the RH schemes have different expressions, they are shown to be a simplified form of the statistical scheme (cf. Smith 1990).

The original Sommeria and Deardorff's (1977) statistical scheme has been proposed for use in mesoscale models, in which the PDF variance varies solely due to turbulence activity. However, in large-scale models such as GCMs, the sources of the PDF variance are not only the turbulence but also other subgrid-scale processes such as advection and cumulus convection. When multiple processes affect the PDF moments, it is difficult to derive diagnostic equations. Moreover, a diagnostic expression is regarded to be an instantaneous adjustment of the subgrid-scale fluctuations, which may not be quite valid. A more physically and computationally desirable method is to replace the diagnostic relationship with the *prognostic* equations for the moments.

The prognostic cloud scheme was first developed by extending the diagnostic RH scheme (Sundqvist et al. 1989; Tiedke 1993; Rasch and Kristjansson 1998; Del Genio et al. 1996). The scheme solves prognostic equations for the grid-mean humidity and cloud water, by dividing a grid box into cloudy and cloud-free parts. Such schemes can easily be implemented in GCMs, but several drawbacks have been pointed out. For example, Gregory et al. (2002) reexamined Sundqvist et al.'s (1989) derivation and showed that the cloud water content calculated using an independent prognostic equation is not consistent with the implicitly assumed PDF based on which the cloud cover is diagnosed. Another drawback is that the cloud fraction is too sensitive to small errors in predicted RH (Xu and Randall 1996). Tiedke's (1993) scheme is often considered to be the archetype of the prognostic cloud scheme; however, it reveals an artificial irreversibility between the cloud production and dissipation under uniform forcing, due to an implicit assumption of the PDF (see Tompkins 2005 for details).

As evident from the above discussion, a favorable cloud parameterization should have consistency between the cloud fraction and the condensate mixing ratio, which is easily achieved with statistical schemes. Recently, such a PDF-based prognostic scheme was proposed by Tompkins (2002, hereafter referred to as T02) who used the beta PDF and solved prognostic equations for the PDF width and shape parameters. He further implemented the scheme in the ECHAM5 atmospheric GCM (AGCM), and demonstrated the ability of the scheme to reduce climatological bias in cloud cover. Another prognostic scheme, called the PC2 scheme, was developed for use in the Hadley Centre GCM (Gregory et al. 2000; Wilson and Gregory 2003; Bushell et al. 2003), which is an elegant extension of the statistical scheme. Namely, power expansion is applied to a PDF in order to evaluate its local derivative near the saturation curve, which is used for prognostic equations to determine the cloud fraction and condensate mixing ratio. The PC2 scheme can also be solved as a prognostic scheme for the PDF moments (Bushell et al. 2003), although special care is required when representing the cloud initiation. Several expensive prognostic schemes that incorporate subgrid-scale vertical motion have been developed (Lappen and Randall 2001; Larson and Golaz 2005); however, they are yet to be applied to large-scale models.

In this study, we introduce a PDF-based prognostic cloud scheme and examine its behaviors in a simple configuration as well as in a global climate simulation with a coarse resolution AGCM. While the scheme proposed in this paper explicitly assumes the subgrid PDF akin to T02, advantage of the Tiedke-type scheme is also incorporated. By means of simpler PDFs that enable us to derive quasi-reversible functions between the cloud fraction and condensates and the PDF moments, the proposed scheme avoids the arbitrariness involved in formulating the source terms to the PDF moments. Hereafter, we refer to the proposed scheme as the hybrid prognostic cloud (HPC) parameterization.

This paper is organized as follows. In Sect. 2, we introduce the framework of the

HPC scheme. The scheme is tested in simple configurations in Sect. 3. The new parameterization is then incorporated into the CCSR/NIES/FRCGC AGCM in Sect. 4. We attempt to verify the PDF moments calculated using the HPC scheme by comparing them with those diagnosed from a global CRM (GCRM). The AGCM run is further extended to obtain climatological fields that are compared with the observations, thus demonstrating that HPC significantly reduces biases not only in cloud cover but also in other fields. The summary and discussion are provided in Sect. 5.

2. Description of the HPC scheme

a. Basis functions for the "s-distribution"

The majority of statistical cloud schemes use the so-called "*s*-distribution", following Sommeria and Deardorff (1977). A single variable *s*, which is a linear combination of the liquid temperature and total water perturbations, is convenient for taking the subgrid-scale fluctuation in both variables into account for condensation. Since the subgrid fluctuation of water is generally dominant over that of the temperature, the latter is sometimes ignored (LeTreut and Li 1991; T02). However, observational evaluations suggest that such simplification may lead to cloud errors in some cases (Price and Wood 2002), so that we adopt the PDF for *s*, denoted as $G(s)$.

For any choice of $G(s)$, the grid-mean cloud fraction, C, and cloud water (including ice) mixing ratio[1], $\overline{q}_c$, are obtained by integrating $G(s)$ and $(Q_c + s)G(s)$, where Q_c denotes the grid-scale saturation deficit defined by (A3), over the saturated part of the grid. For given values of the PDF variance and skewness, denoted by $\mathcal{V}$ and $\mathcal{S}$, respectively, the integrals can be symbolically expressed as

[1] The fast condensation assumption may often break for the cloud ice, but for simplicity we treat it as the cloud liquid water in this paper.

$$C = I_C(\overline{p}, \overline{T_l}, \overline{q_t}, \mathcal{V}, \mathcal{S}) \quad , \tag{1}$$

$$\overline{q_c} = I_q(\overline{p}, \overline{T_l}, \overline{q_t}, \mathcal{V}, \mathcal{S}) \quad , \tag{2}$$

where $\overline{p}$ denotes the pressure, $\overline{T_l}$ the liquid temperature, $\overline{T_l} = \overline{T} - L\overline{q_c}/c_p$, and $\overline{q_t}$ the total water. The overbars denote the grid-mean quantity. The specific humidity is simply written as

$$\overline{q_v} = \overline{q_t} - \overline{q_c} \quad . \tag{3}$$

If the PDF is not too complicated, (1)–(2) can be analytically solved for $\mathcal{V}$ and $\mathcal{S}$ by defining integrand functions, $\tilde{I}$, as

$$\mathcal{V} = \tilde{I}_{\mathcal{V}}(\overline{p}, \overline{T_l}, \overline{q_v}, \overline{q_c}, C) \quad , \tag{4}$$

$$\mathcal{S} = \tilde{I}_{\mathcal{S}}(\overline{p}, \overline{T_l}, \overline{q_v}, \overline{q_c}, C) \quad . \tag{5}$$

The relationship between (1)–(2) and (4)–(5) is quasi-reversible because the cloud fraction and cloud condensates are always consistent with the PDF moments, except for the clear sky (C=0) and the overcast sky (C=1) for which the integrand functions cannot be calculated (cf. T02). It is also noted that $\mathcal{V}$ and $\mathcal{S}$ are conserved for uniform processes that alter solely $\overline{T_l}$ and $\overline{q_t}$ but not the condensate and cloud fraction.

Two PDFs are employed: a double-uniform (DU) function, which assumes uniformity in clear sky and overcast parts separately, and a skewed-triangular (ST) function. These PDFs are regarded to be extensions of the conventional symmetric functions adopted by LeTreut and Li (1991) and Smith (1990), respectively. As stated in the introduction, the abovementioned PDFs are selected because of their feasibility in deriving $\tilde{I}$ and their diagnostic counterparts known to work well in some GCMs despite their simple shapes. Detailed expressions for (1)–(2) and (4)–(5) of these two schemes, denoted as HPC-DU and HPC-ST schemes, respectively, are provided in appendix A.

Fig. 1

Examples of the two PDFs are shown in Fig. 1, with different values of the skewness.

While the ST distribution having a longer tail represents the smooth transition around C=0 and C=1, the DU distribution can represent a larger skew as compared to ST that has a threshold of $\mathcal{S} = \pm 0.57$ when the PDF is a right-angled triangle.

b. Prognostic equations

As the cloud variables are expressed in (1)–(2), the cloud scheme is composed using prognostic equations for four variables determining I, namely, $\overline{T_l}$, $\overline{q_t}$, $\mathcal{V}$, and $\mathcal{S}$. The former two variables are treated in the dynamics part of the GCM, i.e., primitive equations, by modifying the thermodynamic equation with respect to the liquid temperature.

$$\frac{D\overline{T_l}}{Dt} - \frac{\overline{\alpha}\,\overline{\omega}}{c_p} = \frac{Q}{c_p} - \mathcal{D}(\overline{T_l}) \quad , \qquad (6)$$

where D/Dt denotes the total derivative, including three-dimensional advection. Q is the diabatic term and $\mathcal{D}$ represents the horizontal diffusion. The conservation raw of water is written as

$$\frac{D\overline{q_t}}{Dt} = S \quad , \qquad (7)$$

where S denotes the source/sink of water due to surface evaporation and precipitation (including snow fall).

In addition, prognostic equations for the PDF variance and skewness are expressed as

$$\frac{D\mathcal{V}}{Dt} = \left.\frac{\Delta\mathcal{V}}{\Delta t}\right|_{\text{conv.}} + \left.\frac{\Delta\mathcal{V}}{\Delta t}\right|_{\text{micro.}} + \left.\frac{\Delta\mathcal{V}}{\Delta t}\right|_{\text{turb.}} - \varepsilon_{\mathcal{V}} \quad , \qquad (8)$$

$$\frac{D\mathcal{S}}{Dt} = \left.\frac{\Delta\mathcal{S}}{\Delta t}\right|_{\text{conv.}} + \left.\frac{\Delta\mathcal{S}}{\Delta t}\right|_{\text{micro.}} + \left.\frac{\Delta\mathcal{S}}{\Delta t}\right|_{\text{turb.}} - \varepsilon_{\mathcal{S}} \quad , \qquad (9)$$

where subscripts ‘conv.’, ‘micro.’ and ‘turb.’ indicate convective, microphysical and turbulent mixing processes, which all affect the PDF shape. The last terms represent dissipation due to subgrid-scale horizontal motions. The expressions for each term in (8)–(9) are described

below.

1) Cumulus convection

Cumulus convections parameterized in GCMs modify the grid-mean enthalpy and total water by transporting the net moist energy upward. For any type of mass-flux cumulus parameterizations, convective effects are represented as an adiabatic term due to subsidence in the environment, detrainment, and downdraft:

$$\left.\frac{\partial \overline{h}}{\partial t}\right|_{\text{conv.}} = M_c \frac{\partial \overline{h}}{\partial z} + D(h^t - \overline{h}) \quad , \qquad (10)$$

$$\left.\frac{\partial \overline{q}_v}{\partial t}\right|_{\text{conv.}} = M_c \frac{\partial \overline{q}_v}{\partial z} + D(q_v^t - \overline{q}_v) \quad , \qquad (11)$$

$$\left.\frac{\partial \overline{q}_c}{\partial t}\right|_{\text{conv.}} = M_c \frac{\partial \overline{q}_c}{\partial z} + D(q_c^t - \overline{q}_c) \quad , \qquad (12)$$

where $\overline{h} \equiv c_p \overline{T}_l + g\overline{z} + L\overline{q}_t$ is the grid-scale moist static energy, M_c the cumulus mass-flux including downdraft, and D the detrainment mass-flux. The superscript 't' denotes the quantity in the cumulus tower. Increasing the total water content due to detrainment near the top of the cumulus can produce anvil clouds even with the fixed-PDF scheme. In the HPC scheme, such a process first alters the PDF, which then controls the amount and duration of anvil/cirrus clouds during a large-scale condensation (LSC) process. Moreover, the detrainment of the cloudy air mass is included, as in Bushell et al. (2003),

$$\left.\frac{\partial C}{\partial t}\right|_{\text{conv.}} = D(1 - C) \quad . \qquad (13)$$

The vertical transport of a cloudy mass may be included in (13), but it cannot affect the PDF if $C = 1$ throughout the cumulus tower, which may occur frequently. Therefore, this effect is expressed in terms of the PDF moments but not the cloud fraction. The total effect of cumulus convection to the PDF moments is thus written as

$$\left.\frac{\Delta \mathcal{V}}{\Delta t}\right|_{\text{conv.}} = M_c \frac{\partial \mathcal{V}}{\partial z} + \frac{\Delta \tilde{I}_{\mathcal{V}}}{\Delta t} \quad , \qquad (14)$$

$$\left.\frac{\Delta \mathcal{S}}{\Delta t}\right|_{\text{conv.}} = M_c \frac{\partial \mathcal{S}}{\partial z} + \frac{\Delta \tilde{I}_{\mathcal{S}}}{\Delta t} \quad . \qquad (15)$$

The second terms on the rhs of (14)–(15) indicate the changes in the PDF moments consistent with the changes in the grid-scale temperature, humidity, cloud water, and cloud fraction obtained by integrating (10)–(13) over a single time step. This is implemented using the integrand functions (4)–(5) as

$$\Delta \tilde{I}_{\chi} = \tilde{I}_{\chi}(\overline{p}, \overline{T}_l + \Delta \overline{T}_l, \overline{q}_v + \Delta \overline{q}_v, \overline{q}_c + \Delta \overline{q}_c, C + \Delta C) - \tilde{I}_{\chi}(\overline{p}, \overline{T}_l, \overline{q}_v, \overline{q}_c, C) \quad , \qquad (16)$$

where χ is either $\mathcal{V}$ or $\mathcal{S}$.

2) Cloud microphysics

Large-scale condensation should in principle be a part of, and therefore tightly coupled with, cloud microphysical processes. For example, stratiform rainfall preferentially removes the cloud water from the grid box and hence contributes toward the negatively skewed PDF. Since the construction of a microphysics scheme is beyond the scope of this study, we briefly introduce the method to predict the change in PDF due to in-cloud processes other than the condensation and evaporation of clouds treated in Sect. 2a.

In the presence of a partial cloud, the tendency in $\overline{T}_l$ may be expressed as

$$\left.\frac{\partial \overline{T}_l}{\partial t}\right|_{\text{micro.}} = -\frac{L}{c_p}(E - P + \frac{L_m}{L} F) \quad , \qquad (17)$$

where E denotes the evaporation of raindrops plus the sublimation of snow, P the precipitation and snow fluxes, and F the freezing/melting of precipitation/snow. F only appears in (17) because the rain and snow are both diagnostic, and E and P act as source and sink to the water vapor and cloud water.

$$\left.\frac{\partial \overline{q}_v}{\partial t}\right|_{\text{micro.}} = E \quad , \qquad (18)$$

$$\left.\frac{\partial \overline{q}_c}{\partial t}\right|_{\text{micro.}} = -P \quad , \qquad (19)$$

where E is simply expressed as

$$E = k_E \frac{\overline{q}_c}{V_T} F_P \quad , \qquad (20)$$

where F_P denotes the net accumulation of rain and snow water at the layer, V_T the terminal velocity, and k_E the evaporation factor ($V_T = 5$ m s^{-1} and $k_E = 0.5$). The precipitation flux consists of the flux within the layer, $\hat{P}$, and sedimentation of cloud ice above the layer; the former is represented by the autoconversion process, as follows:

$$\hat{P} = \frac{\overline{q}_l}{\tau_p} + \frac{\overline{q}_i}{\tau_s} \quad , \qquad (21)$$

where $\overline{q}_l$ and $\overline{q}_i$ are the cloud liquid and ice partitioned from $\overline{q}_c$, referring to temperature as $\overline{q}_l = (1 - f_i(\overline{T}))\overline{q}_c$ and $\overline{q}_i = f_i \overline{q}_c$, τ_p and τ_s the autoconversion and ice sedimentation time obtained using a Berry-type parameterization (Berry 1967) and a simple function of the ice mixing ratio, respectively.

The tendency due to microphysical processes can be written in a similar manner to the cumulus effect:

$$\left.\frac{\Delta \mathcal{V}}{\Delta t}\right|_{\text{micro.}} = \frac{\Delta \tilde{I}_{\mathcal{V}}}{\Delta t} \quad , \quad \left.\frac{\Delta \mathcal{S}}{\Delta t}\right|_{\text{micro.}} = \frac{\Delta \tilde{I}_{\mathcal{S}}}{\Delta t} \quad , \qquad (22)$$

where $\Delta \tilde{I}_{\mathcal{V}}$ and $\Delta \tilde{I}_{\mathcal{S}}$ follow (16), except that the changes in $\overline{T}_l$, $\overline{q}_v$, and $\overline{q}_c$ are derived from (17)–(19) with $\Delta C = 0$. The expressions (20)–(21) will vary with different microphysics schemes, but the framework of HPC remains valid.

3) Turbulent mixing

Following the studies of Mellor and Yamada (1982) and their extension by Nakanishi and Niino (2004), the time evolution of the subgrid-scale variance and covariance for liquid

potential temperature and total water, both due to turbulence, are derived as

$$\frac{D\overline{\theta_l'^2}}{Dt}-\frac{\partial}{\partial z}\left(lqS_\theta\frac{\partial\overline{\theta_l'^2}}{\partial z}\right)=-2\overline{w'\theta_l'}\frac{\partial\overline{\theta}_l}{\partial z}-\frac{2q}{\Lambda_2}\overline{\theta_l'^2} \quad , \tag{23}$$

$$\frac{D\overline{q_t'^2}}{Dt}-\frac{\partial}{\partial z}\left(lqS_q\frac{\partial\overline{q_t'^2}}{\partial z}\right)=-2\overline{w'q_t'}\frac{\partial\overline{q}_t}{\partial z}-\frac{2q}{\Lambda_2}\overline{q_t'^2} \quad , \tag{24}$$

$$\frac{D\overline{\theta_l'q_t'}}{Dt}-\frac{\partial}{\partial z}\left(lqS_{\theta q}\frac{\partial\overline{\theta_l'q_t'}}{\partial z}\right)=-\overline{w'q_t'}\frac{\partial\overline{\theta}_l}{\partial z}-\overline{w'\theta_l'}\frac{\partial\overline{q}_t}{\partial z}-\frac{2q}{\Lambda_2}\overline{\theta_l'q_t'} \quad , \tag{25}$$

where $q^2=\overline{u'^2+v'^2+w'^2}$ denotes the turbulent kinetic energy (TKE), and the other symbols follow the original notation. Assuming that the TKE production due to buoyancy and vertical shear is balanced with the dissipation term, i.e., the level-2 closure, q is diagnosed as

$$q=\sqrt[3]{\Lambda_1(1-R_f)K_M\left\{\left(\frac{\partial\overline{u}}{\partial z}\right)^2+\left(\frac{\partial\overline{v}}{\partial z}\right)^2\right\}} \quad , \tag{26}$$

where K_M is the turbulent mixing coefficient for momentum and R_f is the flux Richardson number.

From the definition of *s* (see appendix A), the PDF variance becomes

$$\mathcal{V}=a_L^2\left(\overline{q_t'^2}+\alpha_L^2\Pi\overline{\theta_l'^2}-2\alpha_L\Pi\overline{q_t'\theta_l'}\right) \quad , \tag{27}$$

where Π is the Exner function. By using (23)–(27), after some manipulation, the time change of $\mathcal{V}$ can be derived as

$$\left.\frac{\Delta\mathcal{V}}{\Delta t}\right|_{\text{turb.}}=2a_L^2\left[(\alpha_L\Pi)^2K_H\left(\frac{\partial\overline{\theta}_l}{\partial z}\right)^2+K_q\left(\frac{\partial\overline{q}_t}{\partial z}\right)^2-\alpha_L\Pi(K_H+K_q)\frac{\partial\overline{\theta}_l}{\partial z}\frac{\partial\overline{q}_t}{\partial z}\right]-\frac{2q}{\Lambda_2}\mathcal{V} \quad , \tag{28}$$

where K_H and K_q are the mixing coefficients for sensible heat and moisture, respectively,

and both are obtained from the level-2 closure. Since the turbulence production does not affect the PDF shape parameter defined by the third moment (cf. T02), the skewness change $\Delta \mathcal{S}/\Delta t\big|_{\text{turb.}}$ is simply calculated due to the variance change in (28). The inconsistency in the present coupling between the turbulence and the cloud scheme must be noted; turbulence production is diagnostically evaluated using the level-2 closure, which, however, is represented in a prognostic equation in (28). Since the turbulent mixing is only one of the sources of the change in the PDF variance in large-scale models, we must include (27) (diagnosed from the turbulence closure) as a tendency term to the total variance equation (8). By referring to the fast timescale of the turbulence, this inconsistency may not be serious, and can be avoided in future by adopting the level-3 closure of Nakanishi and Niino (2004).

4) Subgrid-scale horizontal eddy

In the planetary boundary layer, the subgrid-scale inhomogeneity is dissipated due to the turbulent mixing. In free atmosphere, the grid box will be homogenized mainly due to mesoscale motions, which are expressed by the Newtonian damping as in T02:

$$\varepsilon_{\mathcal{V}} = \frac{\mathcal{V}}{\tau_h} \quad , \quad \varepsilon_{\mathcal{S}} = \frac{\mathcal{S}}{\tau_h} \quad , \tag{29}$$

where the relaxation timescale is (as it represents the subgrid-scale eddy viscous diffusion) parameterized by the horizontal wind shear as

$$\tau_h^{-1} = C_s^2 \left\{ \left(\frac{\partial \overline{u}}{\partial x} \right)^2 + \left(\frac{\partial \overline{v}}{\partial y} \right)^2 \right\}^{1/2} \quad , \tag{30}$$

where the coefficient C_s is set to 0.23 following T02, which provides τ_h of roughly 10 days for the shear of 2×10^{-5} s^{-1}. Although this representation for eddy dissipation may be too crude, we have confirmed that the PDF moments are not quite sensitive to the terms in (29) when the scheme has been implemented in the AGCM.

5) Note on implementation

The prognostic equations (8)–(9) provide the "memory" for cloud variables beyond a time step. Simultaneously, the cloud variables and the PDF moments maintain consistency based on their quasi-reversible relationship. This means that for each time step before the physics computation, the cloud variables are reset by using (1)–(2). The changes in C and $\overline{q}_c$ that occur due to this resetting arise solely from the grid-scale advection, which is small as compared to the changes due to physical processes, as illustrated in Sect. 4a. This implies that the prognostic equations can also be expressed in terms of C and $\overline{q}_c$ instead of (8)–(9), which is another form of the HPC scheme.

Before presenting the results, we briefly discuss the portability of the scheme. The expressions for the source/sink terms to the PDF moments strongly depend on the other parameterization schemes; however, the core part of HPC, i.e., (1)–(9) does not. Therefore, HPC can be operated in any GCM that calculates tendencies due to convection, microphysics, and turbulence in either terms of a set of $(\overline{q}_t, \overline{q}_c, C)$ or $(\overline{q}_t, \mathcal{V}, \mathcal{S})$.

3. Simple tests for the prognostic scheme

Before implementing the new cloud parameterization in a large-scale model, it will be useful to understand the behavior of the scheme in a simpler framework. In this section, we examine the time evolution of the predicted cloud in two types of idealized experiments, one with a single grid box and another with a single column in which a slightly simple HPC scheme is implemented.

a. Wilson-Gregory test

Wilson and Gregory (2003) proposed a simple test for cloud schemes in order to observe whether they satisfy the necessary conditions of (i) consistency, (ii) reversibility, and (iii) dependence on initial conditions, by using a single grid box forced either by uniform

forcing (e.g., dynamics) or by non-uniform forcing (e.g., precipitation). Condition (i) represents a constraint between the cloud fraction and cloud water; for example, $\overline{q}_c \to 0$ as $C \to 0$, whereas (ii) is achieved if the final state returns to the initial state after uniform cooling followed by uniform warming with the same magnitude. These two conditions are easily satisfied with the statistical scheme, but condition (iii), which requires that the cloud production (dissipation) should not depend on the initial cloud water (saturation deficit), cannot easily be accomplished.

The Wilson-Gregory test is performed using the HPC scheme and conventional diagnostic schemes by LeTreut and Li (1991) and Smith (1990), as follows. We first set initial values of $\overline{T}_l = 273$ K, $\overline{q}_t = q_s(\overline{T}_l)$, $C = 0.5$, and $\overline{q}_c = 0.05$ g kg^{-1}; with these values, the PDF can be defined from (4)–(5) in HPC while the PDF width or variance is fixed in the diagnostic schemes ($b = 0.1$ for the LeTreut and Li scheme and $RH_c = 0.9$ for the Smith scheme). The grid box is then forced by uniform cooling or warming at a rate of 0.002 K s^{-1} until $\overline{T}_l$ varies by ± 2.5 K. The time integration is repeated with a different initial $\overline{q}_c$, but the other variables are not varied.

The main results are presented in appendix A, except for the figure illustrating the $\overline{q}_c - C$ relationship among the four schemes (Fig. 2). In the diagnostic schemes, the PDF variance is prescribed by the constant b or RH_c; hence, the initial cloud fraction is not allowed to remain constant for different initial $\overline{q}_c$, thereby causing the $\overline{q}_c - C$ relationship to be independent of the initial conditions (Fig. 2a,b). In the HPC scheme, for different initial $\overline{q}_c$, the same cloud fraction of $C = 0.5$ can be realized by changing the variance, which is roughly proportional to the condensate mixing ratio (cf. Fig. 16), thereby resulting in different paths of cloud production and dissipation (Fig. 2c,d). This serves larger degrees of freedom in representing cloud optical properties such as thinning or thickening of cloud without changing

Fig. 2

the fraction.

The results in Fig. 2 can be analytically obtained by differentiating (A4)–(A5) and combining them (Wilson and Gregory 2003):

$$C = 1 - \exp\left(-k\overline{q}_c\right) \quad , \tag{31}$$

where $k = G(-Q_c)/\{C(1-C)\}$. The original form of (31) was derived by Wang and Wang (1999); in their expression, the PDF is normalized so that k is replaced with $k/(a_L \mathcal{V}^{1/2})$. This provides a reasonable explanation for the $\overline{q}_c - C$ relationship in the HPC scheme that represents a larger $\partial C / \partial \overline{q}_c$ for a low initial condensate and hence a smaller variance. Wang and Wang (1999) states that k will not be a global constant but will vary depending on the cloud type. In fact, the $\overline{q}_c - C$ relationship obtained from aircraft measurements shows that (31) is broadly fitted but the relationship is considerably scattered (Fig. 5 of Wood and Field 2000). On the basis of these observations, it can be expected that the HPC scheme provides a more favorable simulation of various clouds as compared to fixed-PDF schemes.

b. Single column model test

The Wilson-Gregory test is useful for understanding the basic behavior of the scheme, particularly its core part in (1)–(5). However, the PDF does not change with uniform forcing; therefore, prognostic equations (8)–(9) have to be verified together with other processes in an atmospheric column. Here, we use the single column model (SCM) that incorporates the HPC scheme coupled with cumulus convection and cloud microphysics schemes used in the CCSR/NIES/FRCGC AGCM (see Sect. 4 for the description). Because the SCM lacks surface heat fluxes, we simplify the turbulent mixing by replacing it with a Newtonian damping with a timescale of 3 h, below 2 km. From the initial idealized profiles for temperature and moisture given by Weisman and Klemp (1982), the SCM is integrated for half a day in order

to investigate the change in PDF associated with the deep convection. It must be noted that no initial cloud is considered, and the initial PDF moments are provided from (4)–(5).

Figure 3 shows the time evolution in the SCM using the HPC-DU scheme. The deep convection immediately grows and ceases after approximately 1 h; this accompanies the upper-level ice clouds and lasts for a much longer time (Fig. 3a,b). The associated changes in PDF variance and skewness are found to be distinct before and after the convective cloud is dissipated (Fig. 3c). When the convection is active, the variance increases between 7 and 10 km where the cumulus mass-flux is the strongest, whereas the positive skewness occurs at a higher level mostly due to detrainment of cloud condensates. As the convection decays, a widened and positively skewed PDF corresponds to a lower altitude, following the cumulus top. Simultaneously, a stratiform precipitation selectively removes the condensates, which act to restore the skewness, and furthermore, the subsidence of relatively dry air increases the lower bound of the PDF, thus resulting in a weak negative skew in the upper-levels.

Fig. 3

Because of the initial unstable profile, precipitation is dominated by the convective process (Fig. 3d). The relative dominance of convective and stratiform rainfall varies in response to the initial stability, nevertheless, the overall time evolution of the PDF moments remains unchanged (not shown). Although the convective sources to the PDF moments might actually be highly complex, as suggested by Klein et al. (2005), the SCM results indicate that the HPC scheme represents the most important process, that is, the cumulus detrainment increases both variance and skewness at a thick layer around the cumulus top. Results obtained using the ST scheme are also similar to that in Fig. 3, except that the change in skewness is small (cf. Sect. 2a).

4. Implementation in the AGCM

We have incorporated the HPC scheme into the CCSR/NIES/FRCGC AGCM, which

is an atmospheric component model of MIROC (K-1 model developers 2004). MIROC is one of the two Japanese community climate models, and it has contributed to IPCC AR4 in which the climate sensitivity has been extensively examined. The physical parameterizations coupled to the HPC scheme, as described in the previous section, include the prognostic cumulus convection scheme (Pan and Randall 1993) and the level-2 turbulence closure (Mellor and Yamada 1982). The original CCSR/NIES/FRCGC AGCM employs the diagnostic cloud scheme by LeTreut and Li (1991). To focus on the direct effect of the new cloud scheme, the chemical transport and interactive aerosol modules that have been implemented in MIROC are now excluded.

By using a coarse resolution of T42 with 20 vertical levels, two sets of the AGCM runs were performed. The first run was a set of short one-week integrations starting from December 25, 2006, with the initial and boundary conditions derived from the Japan Meteorological Agency (JMA) operational analysis and the global sea surface temperature (SST) calculated from the AMSR-E satellite. These short integrations were conducted to validate the PDF moments by comparing them with a similar short integration but with a GCRM having a 3.5 km horizontal resolution. The model, referred to as the non-hydrostatic icosahedoral atmospheric model (NICAM, see appendix B for the brief description), provides a powerful reference to the cloud parameterization because the PDF property is largely be dependent on the location and therefore it cannot be justified by comparing with small-domain CRM data.

The second run comprised the 20-year integrations using the HPC (both DU and ST) schemes and the conventional diagnostic scheme. This set aimed at comparing the climatological fields with observations and then evaluating the impact of the new cloud parameterization. The monthly or annual mean climatology was calculated for the last 18 years in each run. To demonstrate the impact of the prognostic treatment of PDF moments, we

performed another 20-year sensitivity experiment using the HPC-DU in which the PDF moments were reset for every time step before the physics calculation. This run, called NOMEM, is compared to the standard run using the HPC-DU scheme and will be shown later in this section.

a. Snapshots of the PDF moments

Figure 4 displays snapshots of the low-level cloud water mixing ratio at 96 h from the initial states. The NICAM data are stored on z surfaces, so that the AGCM fields are interpolated to the z-coordinate. In the AGCM, the cloud water is generally excessive as compared to that in the GCRM, particularly in the tropics. Dense cloud water in the midlatitude is mostly accompanied by extratropical cyclones, which have a very fine structure in NICAM (not shown, but it is clear in an enlarged map). In the AGCM, overestimated cloud water may be inevitable when we focus on reproducing a realistic cloud fraction because the PDFs used in HPC are too simple to represent a long tail of the subgrid-scale fluctuation.

Fig. 4

The PDF variance and skewness obtained with HPC are compared to the corresponding statistics in NICAM (Figs. 5 and 6). For this purpose, the 52 428 800 GCRM grid points in one layer are distributed onto the T42 grid, and then the subgrid-scale variance and skewness of s are calculated.

The variance in NICAM is larger in the lower troposphere and over the low-latitude oceans (Fig. 5a,d). This overall character is well reproduced with the HPC scheme, regardless of the choice of the PDF (Fig. 5b-c,e-f). Figure 5 shows that the AGCM cannot reproduce the variance in the GCRM in several situation, for example, for a large variance around the subtropical stratocumulus regime at z=835 m and a modest variance over the entire subtropics at z=8.3 km.

Fig. 5

Similarly, the HPC scheme can reproduce the PDF skewness in NICAM but with

several discrepancies in the detail (Fig. 6). In NICAM, a negatively skewed PDF is dominant over the ocean at z=835 m, whereas the positive skew is found over most of the tropics at z=8.3 km, except for deep convective regions where the skewness is strongly negative probably due to precipitation (cf. Fig. 3). The skewness distribution obtained from the HPC scheme is reasonable in upper levels, but the positive skewness is underrepresented (Fig. 6d,f). The low-level distribution varies considerably in comparison to NICAM's statistics because the positive skewness is observed as often as the negative one in the tropics (Fig. 6b,c). Despite the discrepancies, the AGCM using the HPC scheme appears to reproduce the PDF moments in the GCRM to a certain extent.

Fig. 6

Since the behavior of the HPC scheme is controlled by the source/sinks terms associated with other physical processes, it is worth examining the budgets for the PDF moments. We select two regions of the western Pacific (100°–150°E, 20°S–20°N) and the eastern off-equatorial Pacific (80°–120°W, 20°S–Eq.) as examples. The initial spin-up period is eliminated so that each tendency term is averaged between 72 and 144 h. In both the regions, the cumulus convection increases the variance above the boundary layer, which is largely compensated by the sink due to microphysical processes (Fig. 7a,b). This is reasonable because the convective detrainment can lead to large spatial inhomogeneity, whereas the precipitating process in a cloud layer reduces it. In the boundary layer, turbulent mixing, including dissipation, is an additional source for the PDF variance. A similar tendency is found for the skewness budgets (Fig. 7c,d); cloud microphysics and turbulence cause the negative and positive skewness, respectively. The cumulus convection plays an opposite role in the free troposphere and the boundary layer, which is probably due to the water vapor being pumped up from the boundary layer (leading to negative skewness), and then converted to cloud water and detrained aloft (leading to positive skewness). Overall, the source and sink terms reveal tendencies we expect, and the small residual is balanced by the grid-scale

Fig. 7

advection term (not shown).

b. Impact on climatology

The mean cloud cover in the AGCM climate experiments is compared with the International Satellite Cloud Climatology Project (ISCCP) cloud cover for 1983–2005 (Rossow and Dueñas 2004). Although figures are not presented, the total cloud cover is briefly described. Our AGCM underrepresents the total cloud cover in the subtropics as in the other GCMs (Zhang et al. 2005). This bias is probably due to complex factors and cannot be corrected even with a prognostic scheme (cf. Del Genio et al. 1996; T02). However, the HPC scheme attempts to reduce the cloud cover biases by enhancing the subtropical thin clouds.

The low-level clouds in ISCCP and AGCM runs are shown in Fig. 8. The low cloud covering the eastern subtropical oceans, as observed in satellite data (Fig. 8a), is better reproduced with the HPC scheme than the conventional diagnostic scheme (Fig. 8d). This is well identified in the longitude-height plot of the mean cloud fraction and cloud water in the southern off-equator (not shown). As shown in Fig. 8b,c, two prognostic schemes result in a quite similar climatology, and the difference between the HPC-DU and diagnostic schemes (Fig. 8d) is more than twice that between the HPC-DU and HPC-ST schemes. Hereafter, we present the climatological fields obtained with the HPC-DU scheme.

Fig. 8

For the LSC process coupled with the cumulus convection, which is essential for the hydrological cycle in the atmosphere, implementing the prognostic cloud scheme affects not only the cloud but also other fields. In particular, the mean precipitation pattern is considerably different between the diagnostic and HPC schemes (Fig. 9). The CCSR/NIES/FRCGC AGCM suffers from a precipitation bias that tends to concentrate near the equator; this is corrected using the HPC scheme, which can reproduce the South Pacific convergence zone reasonably well (Fig. 9a-c). The prognostic scheme generally works to

Fig. 9

suppress the intense convection and hence reduces the precipitation near the equator (Fig. 9d).

The zonally averaged specific humidity is also compared with the ECMWF reanalysis data for 1961–1990 (Uppala et al. 2005; Fig. 10). It is known that the shallow and middle-level convections tend to be underrepresented in the mass-flux parameterization for cumulus convection, thereby leading to a dry bias in the tropical lower troposphere at around 800 hPa (Fig. 10e); this is significantly improved with the HPC scheme (Fig. 10d,f). Fig. 10

It is interesting to show the climatological mean distribution of the PDF moments despite there not being any observational counterpart. Unlike the results shown in Figs. 5 and 6, the climatological pattern of the variance is similar to the mean distribution of either evaporation or precipitation (Fig. 11a-c). In the lower troposphere, the largest variance is found in the subtropics where the mean TKE is the maximum (not shown), indicating that the variance is controlled by turbulence. On the other hand, in the middle and upper troposphere, the variance distribution is similar to the precipitation pattern (Figs. 11b,c), which reflects the dominant effect of convections. Fig. 11

The mean skewness distribution may also be interpreted as a consequence of the cumulus and microphysical effects. Unlike the results shown in Fig.6, negative skewness dominates the climatological mean fields; the horizontal mean values (-0.16, -0.12 and -0.11 for the 800, 600 and 250 hPa levels, respectively) have been removed before plotting Fig. 11d-f. As shown in Fig. 6, the present scheme is not sufficient for representing a tiny fraction of large condensates generating the positively skewed PDF. Yet, relative skew reveals a well-organized distribution. At 850 hPa, the PDF is affected by the convective downdraft transporting drier air into the boundary layer, which may explain the largest negative skewness over the continental convective regions (Fig. 11d). Over the subtropical eastern oceanic basins the relatively positive skew is created, which enhances the low clouds (cf. Fig. 8). Above the boundary layer, the cumulus detrainment and precipitation have competing

effects; the latter dominates in the upper layer as convection ceases (cf. Fig. 3c) and hence results in a negative skewness (Fig. 11e,f).

As explained in Sect. 2, the key features of the HPC scheme are the coupling of the PDF with other subgrid-scale processes and the prognostic formulae; the latter possesses the memory of clouds. It will be of importance to understand the extent to which this memory regulates the climatology of the cloud fields as well as the PDF moments. For this purpose, in Fig. 12 we show the differences between the NOMEM and the control runs. In NOMEM, in the beginning of each physics step, the PDF skewness is set to zero, and the variance is diagnostically obtained with the LeTreut and Li (1991) scheme. It should be noted that the results are rarely dependent on the parameter *b* that determines the initial width of the PDF.

When the memory of the PDF shape is eliminated, the variance is decreased (increased) in the lower (upper) troposphere (Fig. 12a,b). It is not yet clear why the variance changes in such a manner, but the degree of change is as large as the mean variance (Fig. 11a,c). Changes in the cloud fraction are roughly opposite to the variance change; clouds are enhanced over the western-central subtropical oceans at 850 hPa and suppressed over the tropical oceans at 200 hPa and over the eastern subtropics at 850 hPa. This is quite consistent with the deduction from (31), which states that the cloud is produced faster when the variance is smaller (cf. Sect. 3a and appendix A). Although the mean cloud distribution can be tuned to some extent, Fig. 12c clearly indicates that the HPC scheme having PDF memory provides better simulation of the subtropical low clouds.

5. Summary and discussion

For better representation of clouds in GCMs, we developed a parameterization for non-convective clouds and condensate mixing ratio on the basis of prognostic equations for the PDF moments ($\mathcal{V}$ and $\mathcal{S}$) of the subgrid-scale water and temperature fields. This

parameterization, called the HPC scheme, is built upon the conventional statistical cloud scheme, but the PDF shape varies both in space and in time due to processes such as cumulus convection, cloud microphysics, and turbulence. Quasi-reversible operators between the grid-scale variables (e.g., cloud fraction) and the PDF moments are the essence of the HPC scheme, which enable us to construct a feasible coupling between the LSC and other physical processes. To achieve this, we employed simple basis PDFs, which can be regarded as an extension of the conventional diagnostic schemes.

Simple tests for HPC show its physically reasonable behavior. As expected, the prognostic PDF serves a memory for clouds with different optical properties (Sect. 3a). Furthermore, coupling with the cumulus convection produces a positively skewed PDF when an anvil cloud is formed, as hypothesized by T02 (Sect. 3b). When the HPC scheme is implemented in the CCSR/NIES/FRCGC AGCM, the model yields a rich distribution of $\mathcal{V}$ and $\mathcal{S}$ qualitatively in a manner similar to those diagnosed from the GCRM simulation, thus supporting that the formulae are physically relevant (Sect. 4a).

Climatological experiments conducted using the T42 AGCM incorporating the HPC scheme reveal that the error in the cloud cover is reduced in comparison to the climatology in the AGCM using the conventional diagnostic scheme. Since the HPC scheme affects the moisture and hence the convective activity as well, the mean patterns of precipitation and zonal-mean specific humidity are better reproduced. While changes in the climate sensitivity are yet to be examined in the forthcoming studies, we expect that the new scheme can represent changes in the cloud optical properties, which would then lead to a response of the cloud-radiative forcing to the parameter change without changing the cloud cover.

It may be argued that simple PDFs employed in this study are too simple to represent the observed PDF (e.g., Wood and Field 2000). However, the results in Sect. 4 exhibit that the climatological mean states are very close to each other in the HPC-DU and -ST schemes and

significantly different from those in the diagnostic scheme. This indicates that the prognostic treatment of the PDF moments has a larger impact on the model climate, rather than the choice of the basis PDF. The HPC scheme can employ other PDFs as far as $\tilde{I}$ can be analytically or numerically obtained; hence, such a test may be worth performing elsewhere.

In the present HPC scheme, $\overline{q}_c$ is assumed to include both liquid and ice phases of condensates. However, the cloud ice is not necessarily suitable for the statistical scheme that assumes the fast condensation. We are currently testing the microphysics scheme proposed by Wilson and Ballard (1999), which is then combined with HPC, in which the cloud ice is predicted using a separate prognostic equation that allows the supersaturation of ice.

We have shown that the PDF-based prognostic scheme represents larger degrees of freedom between the cloud fraction and condensates mixing ratio. This improves the ability of GCMs, as demonstrated thus far, but it may produce a worse climate simulation. Because the HPC scheme explicitly couples the subgrid-scale processes, an error in one process (e.g., turbulence) strongly influences other processes and potentially results in unrevealed biases of the model. For example, the cloud cover distribution obtained from HPC was comparable to the observations, but excessive subtropical clouds occurred over the western-central basin due to a loose representation of the low-level stratification, which can be corrected by improving the turbulent mixing but not the LSC. It is apparent that the HPC scheme stimulates and provides better representation of the subgrid-scale phenomena in large-scale models.

APPENDIX

a. Integral and integrand functions of the PDF

The well-established formulae for the "s-distribution" scheme is briefly described here. By means of the fast condensation assumption, the cloud water in an air parcel can be written as $q_c = (q_t - q_s)\delta(q_t - q_s)$, where q_s denotes the saturation mixing ratio and $\delta(x)$ denotes the Heviside function of x. The right-hand-side of the equation is then approximated with the first order Taylor expansion with respect to an area average quantity $(\bar{})$, thus yielding the following expression:

$$q_c = \begin{cases} Q_c + s & \text{for} \quad -Q_c < s \\ 0 & \text{for} \quad -Q_c \geq s \end{cases} \quad , \qquad \text{(A1)}$$

where

$$s = a_L(q_t' - \alpha_L T_L') \qquad \text{(A2)}$$

is a conservative variable on the liquid temperature-total water plane deviated from the area-averaged saturation deficit defined as

$$Q_c \equiv a_L\left\{\bar{q}_t - q_s(\bar{T}_L, \bar{p})\right\} \quad , \qquad \text{(A3)}$$

where

$$a_L = 1/(1 + L\alpha_L / c_p) \ , \quad \alpha_L = \partial q_s / \partial T\big|_{T=\bar{T}_L} \quad .$$

When the distribution of s in the area follows a PDF $G(s)$, the area-averaged (or grid-scale) cloud fraction and cloud water are obtained by integrating $G(s)$ and $(Q_c + s)G(s)$ over the saturated sub-space, respectively.

$$C = \int_{-Q_c}^{\infty} G(s)ds \quad , \qquad \text{(A4)}$$

$$\bar{q}_c = \int_{-Q_c}^{\infty} (Q_c + s)G(s)ds \quad . \qquad \text{(A5)}$$

The second and third moments of the PDF are given as

$$\mu_2 \equiv \mathcal{V} = \int_{-\infty}^{\infty} s^2 G(s) ds \quad , \qquad \text{(A6)}$$

$$\mu_3 \equiv \mu_2^{3/2} \mathcal{S} = \int_{-\infty}^{\infty} s^3 G(s) d\, s \quad . \qquad \text{(A7)}$$

As mentioned in Sect. 2a, we use two different PDFs in the HPC scheme, providing respectively a different form of (1)–(5), as specified below.

1) Double-uniform PDF (HPC-DU)

The HPC-DU scheme uses two uniform PDFs adjoined at the saturation point, $s = -Q_c$; the widths defined by positions of the right and left edges on the *s*-coordinate are denoted as a and b, respectively. The PDF is expressed as

$$G(s) = \begin{cases} \dfrac{Q_c - a}{(b + Q_c)(b - a)} & \text{for} \quad -Q_c < s \le b \\ \dfrac{Q_c - b}{(a + Q_c)(b - a)} & \text{for} \quad a < s \le -Q_c \end{cases} \quad , \qquad \text{(A8)}$$

and (A4)–(A5) becomes using (A8)

$$C = \begin{cases} 0 & \text{if} \quad b + Q_c < 0 \quad \text{or} \quad Q_c - a < 0 \\ 1 & \text{if} \quad a + Q_c > 0 \quad \text{or} \quad Q_c - b > 0 \\ \dfrac{Q_c - a}{b - a} & \text{else} \end{cases} \quad , \qquad \text{(A9)}$$

$$\overline{q}_c = \begin{cases} 0 & \text{if} \quad b + Q_c < 0 \quad \text{or} \quad C_c - a < 0 \\ \dfrac{b + Q_c}{2} & \text{if} \quad a + Q_c > 0 \quad \text{or} \quad Q_c - b > 0 \\ \dfrac{C(b + Q_c)}{2} & \text{else} \end{cases} \quad . \qquad \text{(A10)}$$

The PDF moments are also written in terms of a and b.

$$\mu_2 = \{Q_c(a+b) - ab\}/3 \quad , \quad \mu_3 = (a+b)\left\{Q_c(a+b) - Q_c^2 - a\right\}b/3 \quad . \qquad \text{(A11)}$$

When a set of the grid-scale variables, $\overline{q}_t$, $\overline{T}_L$, and $\overline{p}$, are given together with $\mathcal{V}$ and $\mathcal{S}$, we can solve (A11) for the PDF parameters as

$$a=\left(\delta-\sqrt{\delta^2-4\varphi}\right)\Big/2\ ,\ b=\left(\delta+\sqrt{\delta^2-4\varphi}\right)\Big/2 \quad , \qquad \text{(A12)}$$

where $\delta\equiv a+b=\mu_3\Big/\left(\mu_2-Q_c^2/3\right)$ and $\varphi\equiv ab=Q_c\delta-3\mu_2$.

It is noted that the square root in (A12) is ensured to be real, and for a symmetric case $\delta=0$ and $\varphi=-3\mu_2$ yield $a=-\sqrt{3\mu_2}$ and $b=\sqrt{3\mu_2}$. Thus, a set of (A9)–(A10) with the aid of (A12) provides integral functions (1)–(2).

Conversely, (A9)–(A10) can be solved for the PDF parameters, as follows:

$$a=\left(Q_c-bC\right)\Big/\left(1-C\right)\quad\text{for}\quad C\neq 1\ ,\quad b=\left(2q_c-Q_cC\right)\Big/C\quad\text{for}\quad C\neq 0\ . \qquad \text{(A13)}$$

They are then substituted into (A11) in order to obtain the integrand functions (4)–(5). It is apparent that $\tilde{I}_V$ and $\tilde{I}_S$ cannot be determined for C=0 or C=1 as the PDF information is partially lost when the source term for the variance and skewness expressed by (16) is set to zero.

2) Skewed-triangular PDF (HPC-ST)

The HPC-ST scheme is derived in a manner similar to that for the HPC-DU scheme. The position of the top, denoted as q, is constrained by

$$a+b+q=0\ ; \qquad \text{(A14)}$$

by definition, $q\le b$ and $a\le q$ must be satisfied. The PDF is then

$$G(s)=\begin{cases}-\dfrac{2(s-b)}{(b-q)(b-a)} & \text{for}\quad q<s\le b\\ \dfrac{2(s-a)}{(q-a)(b-a)} & \text{for}\quad a<s\le q\end{cases}\ , \qquad \text{(A15)}$$

and (A4)–(A5) are

$$C=\begin{cases} 0 & \text{if} \quad b<-Q_c \\ \dfrac{(Q_c+b)^2}{(b-q)(b-a)} & \text{if} \quad q\le -Q_c\le b \\ 1-\dfrac{(Q_c+a)^2}{(q-a)(b-a)} & \text{if} \quad a\le -Q_c\le q \\ 1 & \text{if} \quad -Q_c<a \end{cases} \quad , \qquad \text{(A16)}$$

$$\overline{q}_c=\begin{cases} 0 & \text{if} \quad b<-Q_c \\ \dfrac{1}{3}C(Q_c+b) & \text{if} \quad q\le -Q_c\le b \\ Q_c-\dfrac{1}{3}(1-C)(Q_c+a) & \text{if} \quad a\le -Q_c\le q \\ Q_c & \text{if} \quad -Q_c<a \end{cases} \quad . \qquad \text{(A17)}$$

Substituting (A2) and (A14)–(A15) into (A6)–(A7) leads to the PDF moments expressed in terms of a and b.

$$\mu_2=\{(a+b)^2-ab\}/6 \quad , \quad \mu_3=-ab(a+b)/10 \quad . \qquad \text{(A18)}$$

For the symmetric PDF of $q=0$ and $a=-b$, it is easily shown that $b=\sqrt{6\mu_2}$ thereby (A16)–(A17) reduces to the Smith (1990) scheme.

As in HPC-DU, the PDF parameters a and b can be determined from (A18) for given values of $\overline{q}_t$, $\overline{T}_L$, $\overline{p}$, $\mathcal{V}$, and $\mathcal{S}$:

$$a=2\sqrt{2\mu_2}\cos\left(\frac{1}{3}\cos^{-1}\delta+\frac{2}{3}\pi\right) \ , \ b=2\sqrt{2\mu_2}\cos\left(\frac{1}{3}\cos^{-1}\delta\right) \quad , \qquad \text{(A19)}$$

where $\delta\equiv 5\mu_3\big/(2\mu_2)^{3/2}$.

If $|\delta|$ is greater than unity, (A19) cannot be used; therefore, the third moment is adjusted to a critical value of $\mu_3=\mu_3^{\text{crit}}=\pm\left(2\sqrt{2}/5\right)\mu_2^{3/2}$ when the PDF corresponds to the right-angled triangle of either $q=a$ or $q=b$.

For given $\overline{q}_t$, $\overline{T}_L$, $\overline{p}$, C, and $\overline{q}_c$, the PDF parameters are derived from (A16)-(A17):

$$\left.\begin{aligned} a &= \frac{3(Q_c-\overline{q}_c)}{1-C}-Q_c \\ b &= \frac{1}{2}\left(-a+\sqrt{9a^2-4\frac{(Q_c+a)^2}{1-C}}\right) \end{aligned}\right\} \quad \text{for} \quad a \le -Q_c \le q \quad , \qquad \text{(A20)}$$

$$\left.\begin{aligned} b &= \frac{3\overline{q}_c}{C}-Q_c \\ a &= \frac{1}{2}\left(-b-\sqrt{9b^2-4\frac{(Q_c+b)^2}{C}}\right) \end{aligned}\right\} \quad \text{for} \quad q \le -Q_c \le b \quad . \qquad \text{(A21)}$$

From (A14), (A18), and (A20)–(A21) the expression for $\tilde{I}_V$ and $\tilde{I}_S$ is obtained. These integrand functions are calculated only for $0<C<1$; otherwise $\Delta\tilde{I}_V = \Delta\tilde{I}_S = 0$. Furthermore, it is possible that the PDF parameters calculated using either (A20) or (A21) do not satisfy the associated conditions. In such a case, a PDF cannot be obtained for a given set of the variables. We adjust only the cloud fraction in this particular case as it is independent from the conservation of water.

The adjustment is conducted as follows. From a critical conditions of (A20)–(A21),

$$\begin{aligned} &9b^2-4(Q_c+b)^2/C && \text{for} \quad q \le -Q_c \le b \\ &9a^2-4(Q_c+a)^2/(1-C)=0 && \text{for} \quad a \le -Q_c \le q \end{aligned} \quad ,$$

a and b are removed by substituting (A16)–(A17). After some manipulation, we obtain

$$\gamma^2 = \begin{cases} -4R\sinh^2\left(\frac{1}{3}\sinh^{-1}\left(1/\sqrt{-R}\right)\right) & \text{for} \quad R<0 \\ 4R\cosh^2\left(\frac{1}{3}\cosh^{-1}\left(1/\sqrt{R}\right)\right) & \text{for} \quad 0 \le R<1 \\ 4R\cos^2\left(\frac{1}{3}\cos^{-1}\left(1/\sqrt{R}\right)+\frac{4}{3}\pi\right) & \text{for} \quad 1 \le R \end{cases} \quad , \qquad \text{(A22)}$$

where

$$\begin{aligned} &\gamma=\sqrt{C} \quad , \quad R=\overline{q}_c/Q_c && \text{for} \quad q \le -Q_c \le b \\ &\gamma=\sqrt{1-C} \quad , \quad R=1-\overline{q}_c/Q_c && \text{for} \quad a \le -Q_c \le q \end{aligned}$$

As in the adjustment of μ_3 in (A19), this procedure results in the critical PDF shape

of $q = a$ or $q = b$.

3) Additional simple tests

For understanding the behavior of the HPC-DU and -ST schemes without an explicit implementation of the prognostic moment equations (8)–(9), some additional results of the Wilson-Gregory test are presented in Figs. 13 and 14. As shown in Fig. 2, a single grid box is forced by uniform heating and cooling with different initial $\overline{q}_c$, and then the path of cloud fraction change is compared with the corresponding diagnostic schemes of LeTreut and Li (1991) and Smith (1990). Fig. 13

In the statistical scheme with a fixed PDF shape, the cloud fraction is uniquely determined with respect to a condensate content because there is no freedom allowed between the two variables (Fig. 2a,b). This implies that the dependence on the initial $\overline{q}_c$ is represented simply as a parallel shift in the initial C and its path in LeTreut and Li (1991) and Smith (1990) schemes (Fig. 13a,b). On the other hand, the HPC scheme can represent a less initial $\overline{q}_c$ with a prescribed initial C by providing a PDF that has smaller variance and negative skewness, and vice versa; the former (latter) PDF represents an optically thin (thick) cloud. Hence, the cloud rapidly (slowly) dissipates to the uniform warming, thereby satisfying the condition (iii) described in Sect. 3a (Fig. 13c,d). One caveat to the HPC schemes is that the path for the cloud production also depends on the initial $\overline{q}_c$, which is an unrealistic behavior. As discussed by Wilson and Gregory (2003), for the explicit PDF assumption in which the total water is redistributed implicitly in the grid box, the cloudy and cloud-free areas affect each other, and the false behavior cannot be avoided.

A similar test but with a precipitation process is performed. The precipitation flux is expressed by (21), where we simply set $\tau_p = \tau_s = 15$ min. To emphasize the change in cloud property, the path of the in-cloud water $\overline{q}_c / C$ is shown in Fig. 14. It is found that in LeTreut Fig. 14

and Li (1991) and Smith (1990), the $\overline{q}_c / C$ change is insensitive to the precipitation process when the cloud is dissipated, whereas $\overline{q}_c / C$ is reduced with precipitation when the cloud is produced (Fig. 14a,b). The change in $\overline{q}_c / C$ due to precipitation is larger in the HPC scheme, where the PDF shape is time dependent (Fig. 14c,d). Since the precipitation removes only the condensates, the PDF is eventually skewed to be negative. Such a change in the PDF explains the reduction in $\overline{q}_c / C$ due to precipitation in both the phases of the cloud production and dissipation. These differences between the diagnostic and prognostic schemes are consistent with those obtained by Wilson and Gregory (2003), who showed that the prognostic scheme exhibits a more ideal behavior.

A different behavior of HPC-DU against the LeTreut and Li (1991) scheme and HPC-ST against the Smith (1990) scheme is accomplished by the integrand functions (4)–(5), which may vary initially and evolve in time. The question of how the PDF variance and skewness depend on the grid-scale variables is crucial and is visible by plotting $\tilde{I}_V$ and $\tilde{I}_S$ on the $\overline{q}_c - C$ plane (Fig. 15). The overall property is the same between the two schemes; the variance is highly dependent on $\overline{q}_c$, whereas the skewness mostly varies with C. The above parameters are relatively insensitive to change in $\overline{q}_t$, and the variance increases with decrease in $\overline{q}_t$ (and hence $\overline{q}_v$), representing that drier cloud-free area coexisting with clouds leads to a wider distribution. Furthermore, the skewness change, $\Delta\tilde{I}_S$, to increasing cloud water is negative for sufficient $\overline{q}_t$ but positive for deficient $\overline{q}_t$ (top-right and bottom-right in Fig. 15). The latter condition is often observed in the AGCM when the cumulus detrainment occurs in the middle and upper troposphere (cf. Fig. 3).

Fig. 15

At $C \approx 0$ or $C \approx 1$, a large error in variance occurs along a tiny (mostly numerical) error in $\overline{q}_c$ and/or C (Fig. 15, left). Although HPC-ST does not reveal such sensitivity in

variance, the skewness changes drastically in such situations as in the HPC- DU scheme (Fig. 15, right), which may be significantly uncertain. Therefore, we define a small number, ε, set to 1×10^{-15} and solve $\Delta\tilde{I}_V$ and $\Delta\tilde{I}_S$ only for $\varepsilon < C < 1-\varepsilon$; otherwise the grid box is re-evaluated as a clear sky or overcast sky.

b. Global cloud resolving model

The GCRM used in Sect. 4a has been developed for the first global simulations with explicit cloud microphysics on the Earth Simulator. The model, NICAM, employs a set of governing equations for a fully compressive fluid on the icosahedral grids and implements the bulk microphysical parameterization for cold rain. Readers may refer to Satoh et al. (2008) as the reference to the details on NICAM.

The experimental setup for the one-week integration starting from December 25, 2006, follows Miura et al. (2007). The initial conditions were prepared from the NCEP Tropospheric Analysis on a 1°×1° grid by using the linear interpolation. Similarly, the boundary conditions of the SST and topography are taken from the Reynolds SST and GTOPO30 data, respectively. Although the horizontal spacing is surprisingly fine, the behavior of the simulated clouds still depends on the other subgrid-scale parameterization, which is carefully tuned (Miura et al. 2007). Thorough analyses of the NICAM simulation show that the model appropriately reproduces the super cluster embedded in the Madden-Julian oscillation observed in December, 2006.

Acknowledgments. The authors are grateful to Damian Wilson and two anonymous reviewers for their constructive comments. This work was partly supported by the Global Environmental Research Fund RF-061 by the Ministry of the Environment, Japan. The GCRM simulations were performed using the Earth Simulator, supported by CREST/JST and

the Kakushin project.

REFERENCES

Berry EX (1967) Cloud droplet growth by collection. J Atmos Sci 24: 688-701

Bony S, Dufresne JL (2005) Marine boundary layer clouds at the heart of tropical cloud feedback uncertainties in climate models. Geophys Res Lett 32: L20806, doi:10.1029/2005GL023851

Bougeault P (1981) Modeling the trade-wind cumulus boundary layer. Part I: Testing the ensemble cloud relations against numerical data. J Atmos Sci 38: 2414-2428

Bougeault P (1982) Cloud-ensemble relations based on the Gamma probability distribution for the higher-order models of the planetary boundary layer. J Atmos Sci 39: 2691-2700

Bushell AC, Wilson DR, Gregory D (2003) A description of cloud production by non-uniformly distributed processes. Q J R Meteor Soc 129: 1435-1455

Del Genio AD, Yao MS, Kovari W, Lo K (1996) A prognostic cloud water parameterization for global climate models. J Clim 9: 270-304

Gregory D, Wilson DR, Bushell AC (2002) Insights into cloud parameterization provided by a prognostic approach. Q J R Meteor Soc 128: 1485-1504

K-1 model developers (2004) K-1 coupled model (MIROC) description. In: Hasumi H, Emori S (edn) K-1 technical report. Center for Climate System Research, University of Tokyo, 34pp [available at http://www.ccsr.u-tokyo.ac.jp/~agcmadm/]

Klein SA, Pincus R, Hannay C, Xu KM (2005) How might a statistical cloud scheme be coupled to a mass-flux convection scheme? J Geophys Res 110: D15S06, doi:10.1029/2004JD005017

Lappen CL, Randall DA (2001) Toward a unified parameterization of the boundary layer and moist convection. Part I. A new type of mass-flux model. J Atmos Sci 58**:** 2021–2036

Larson VE, Golaz JC (2005) Using probability density functions to derive consistent closure relationships among higher-order moments. Mon Weather Rev 133: 1023-1042

Lewellen WS, Yoh S (1993) Binormal model of ensemble partial cloudiness. J Atmos Sci 50: 1228-1237

Lohmann U, McFarlane N, Levkov L, Abdella K, Albers F (1999) Comparing different cloud schemes of a single column model by using mesoscale forcing and nudging technique. J Clim 12: 438-461

Le Treut H, Li ZX (1991) Sensitivity of an atmospheric general circulation model to prescribed SST changes: Feedback effects associated with the simulation of cloud optical properties. Clim Dyn 5: 175-187

Mellor GL (1977) The Gaussian cloud model relations. J Atmos Sci 34: 356-358

Mellor GL, Yamada T (1982) Development of a turbulence closure model for geophysical fluid problems. Rev Geophys Space Phys 20: 851-875

Miura H, Satoh M, Nasuno T, Noda A, Oouchi K (2007) A Madden-Julian oscillation event realistically simulated by a global cloud-resolving model. Science 318: 1763-1765

Nakanishi M, Niino H (2004) An improved Mellow-Yamada level-3 model with condensation physics: its design and verification. Bound Layer Meteor 112: 1-31

Pan DM, Randall DA (1998) A cumulus parameterization with a prognostic closure. Q J R Meteor Soc 124: 949-981.

Price JD, Wood R (2002) Comparison of probability density functions for total specific humidity and saturation deficit humidity, and consequences for cloud parameterization. Q J R Meteor Soc 128: 2059-2072.

Rasch PJ, Kristjansson JE (1998) A comparison of the CCM3 model climate using diagnosed and predicted condensate parameterizations. J Clim 11: 1587-1614.

Ricard JL, Royer JF (1993) A statistical cloud scheme for use in an AGCM. Ann Geophys 11: 1095-1115

Rossow WB, Dueñas EN (2004) The International Satellite Cloud Climatology Project (ISCCP) web site-An online resource for research. Bull Amer Meteor Soc 85: 167-176

Satoh M, Matsuno T, Tomita H, Miura H, Nasuno T, Iga S (2008) Nonhydrostatic icosahedral atmospheric model (NICAM) for global cloud resolving simulations. J Comp Phys 227: 3486-3514

Slingo J (1987) The development and verification of a cloud prediction scheme for the ECMWF model. Q J R Meteor Soc 113: 899-927

Smith RNB (1990) A scheme for predicting layer clouds and their water content in a general circulation model. Q J R Meteor Soc 116: 435-460

Sommeria G, Deardorff JW (1977) Subgrid-scale condensation in models of nonprecipitating clouds. J Atmos Sci 34: 344-355

Sundqvist H (1978) A parameterization scheme for non-convective condensation including prediction of cloud water content. Q J R Meteor Soc 104: 677-690

Sundqvist H, Berge E, Kristjansson JE (1989) Condensation and cloud parameterization studies with a mesoscale numerical weather prediction model. Mon Weather Rev 117: 1641-1657

Tiedke M (1993) Representation of clouds in large-scale models. Mon Weather Rev 121: 3040-3061

Tompkins AM (2002) A prognostic parameterization for the subgrid-scale variability of water vapor and clouds in large-scale models and its use to diagnose cloud cover. J Atmos Sci 59: 1917-1942

Tompkins AM (2005) The parameterization of cloud cover. ECMWF Technical Memorandum. 23pp. [available at http://www.ecmwf.int/publications/]

Uppala SM, Co-authors (2005) The ERA-40 re-analysis. Q J R Meteor Soc 131: 2961-3012

Wang S, Wang Q (1999) On condensation and evaporation in turbulence cloud parameterizations. J Atmos Sci 56: 3338-3344.

Weisman ML, Klemp JB (1982) The dependence of numerically simulated convective storms on vertical wind shear and buoyancy. Mon Weather Rev 110: 504-520

Wilson DR, Ballard SP (1999) A microphysically based precipitation scheme for the UK Meteorological Office unified model. Q J R Meteor Soc 125: 1607-1636

Wilson DR, Gregory D (2003) The behaviour of large-scale model cloud schemes under idealized forcing. Q J R Meteor Soc 129: 967-986

Wood R, Field PR (2000) Relationships between total water, condensed water, and cloud fraction in stratiform clouds examined using Aircraft data. J Atmos Sci **57**: 1888-1905

Xu KM, Randall DA (1996) A semiempirical cloudiness parameterization for use in climate models. J Atmos Sci 53: 3804-3102

Zhang MH, Coauthors (2005) Comparing clouds and their seasonal variations in 10 atmospheric general circulation models with satellite measurements. J Geophys Res 110: doi:10.1029/2004JD05021

FIGURE CAPTIONS

Fig. 1 Example of the basis PDF for HPC: **a** double-uniform and **b** skewed-triangular functions. The PDF variance is fixed to 1.33×10^{-2} g^2 kg^{-2}, but the skewness is 0 (solid), 0.4 (thick dashed), 0.8 (thick long dashed), -0.4 (thin dashed) and -0.8 (thin long dashed). The PDF is not plotted for larger skewness in **b** because it is beyond the critical value.

Fig. 2a-d Cloud fraction against cloud water (g kg^{-1}) in the Wilson-Gregory test: **a** LeTreut and Li, **b** Smith, **c** HPC-DU and **d** HPC-ST schemes. The dots with different gray scale indicate the results for different initial cloud water. In **a-b**, the parameters of b=0.1 and RHc=0.9 are used. See text for further details.

Fig. 3a-d Time evolution in the SCM: **a** cumulus mass-flux (shading) and cloud fraction (contour), **b** cloud liquid water (solid contour) and ice (dashed contour) mixing ratio, **c** PDF variance (thin solid contour) and skewness (thick contour) and **d** convective (solid) and stratiform (dashed) precipitation. The contour interval is 0.02 and 0.05 g kg^{-1} for liquid and ice in **b**, 0.1 g^2 kg^{-2} and 0.5 in **c**. The shaded area in **c** indicates positive skewness.

Fig. 4a-d Snapshots of the low-level (z=835 m) cloud water mixing ratio (g kg^{-1}) at 96 h, staring from December 25, 2006: **a** GCRM, **b-c** AGCM with HPC-DU and -ST schemes, respectively.

Fig. 5a-f Same as Fig. 4 but for the PDF variance: **a-c** z=835 m and **d-f** z=8300 m.

Fig. 6a-f Same as Fig. 4 but for the PDF skewness: **a-c** z=835 m and **d-f** z=8300 m.

Fig. 7a-d Regionally averaged tendency terms for the PDF variance: **a** western Pacific (100-150E, 20S-20N), **b** eastern off-equatorial Pacific (80-120W, 20S-EQ). The unit is 10^{-6} g^2 kg^{-2} s^{-1} while the dashed, dotted and solid lines denote the tendency due to cumulus, microphysics and turbulence, respectively. **c-d** Same as **a-b** but for the PDF skewness. The unit is 10^{-5} s^{-1}. All the terms are averaged during 72-144 h.

Fig. 8a-c Annual and climatological mean low cloud cover, observed and modeled: **a** ISCCP, **b** HPC-DU, **c** HPC-ST, **d** difference between HPC-DU and the diagnostic scheme (the former minus latter). The contour interval is 0.1 in **a-c** while 0.05 in **d**, negative contours dashed, and light shading denotes values greater than 0.1.

Fig. 9a-f Annual and climatological mean precipitation, observed and modeled: **a** CMAP, **b** diagnostic cloud scheme, **c** HPC-DU, **d** difference between HPC-DU and the diagnostic scheme, **e-f** biases, i.e., differences between **b-c** and **a**. The contour interval is 2 mm day^{-1} in **d-f** while the shading denotes negative values.

Fig. 10a-f Same as Fig. 9 but for the zonal mean specific humidity. The contour interval in is 2 g kg^{-1} in **a-c** while 0.3 g kg^{-1} in **d-f**. The light (dark) shading in **d-f** denotes the difference or bias greater than 0.5 g kg^{-1} (less than-0.5 g kg^{-1}).

Fig. 11a-f Annual and climatological mean of the PDF moments: **a-c** variance and **d-f** skewness at 850 (upper), 600 (middle), 250 hPa (lower) levels. The contour interval is 3, 1 and 0.1×10^{-2} g^2 kg^{-2} in **a-c** while 0.05 in **d-f**. The shading indicates positive skewness. Note that the horizontal average has been removed in **d-f**.

Fig. 12a-d Differences in the annual and climatological mean fields between NOMEM and the control runs (the former minus latter): **a-b** PDF variance at the 850 and 250 hPa levels, **c-d** cloud fraction at the 850 and 250 hPa levels. The contour interval is 3 and 0.1×10^{-2} g^2 kg^{-2} in **a-b** while 0.05 in **c-d**. The light (dark) shading indicates the difference greater than +0.1 (less than -0.1).

Fig. 13a-d Cloud fraction against temperature change (K) in the Wilson-Gregory test: **a** LeTreut and Li, **b** Smith, **c** HPC-DU and **d** HPC-ST schemes. Lines with different gray scale indicate the results from different initial cloud water. In **a-b** parameters of b=0.1 and RHc=0.9 are used. See text for further details.

Fig. 14a-d Same as Fig. 13 but for the in-cloud condensate contents (g kg^{-1}). The solid and

dashed lines correspond to the results with and without precipitation process, respectively.

Fig. 15 Dependence of the PDF variance (left) and skewness (right) on the total and cloud water contents and the cloud fraction in the HPC-DU scheme. The contour interval is 0.5 g^2 kg^{-2} for the variance while 0.5 for the skewness. The negative contours are dashed. The other variables are fixed at standard initial values for the Wilson-Gregory test.

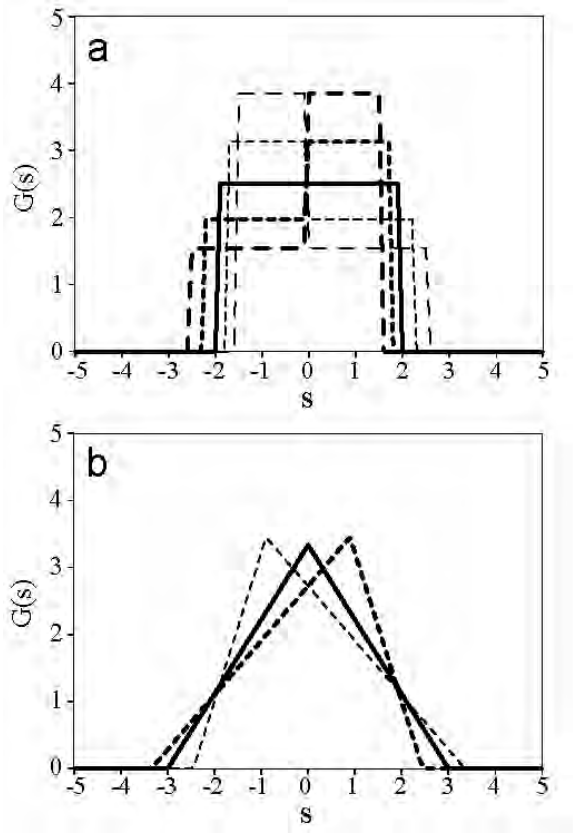

Fig. 1 Example of the basis PDF for HPC: **a** double-uniform and **b** skewed-triangular functions. The PDF variance is fixed to 1.33×10^{-2} g^2 kg^{-2} but the skewness is 0 (solid), 0.4 (thick dashed), 0.8 (thick long dashed), -0.4 (thin dashed) and -0.8 (thin long dashed). The PDF is not plotted for larger skewness in **b** because it is beyond the critical value.

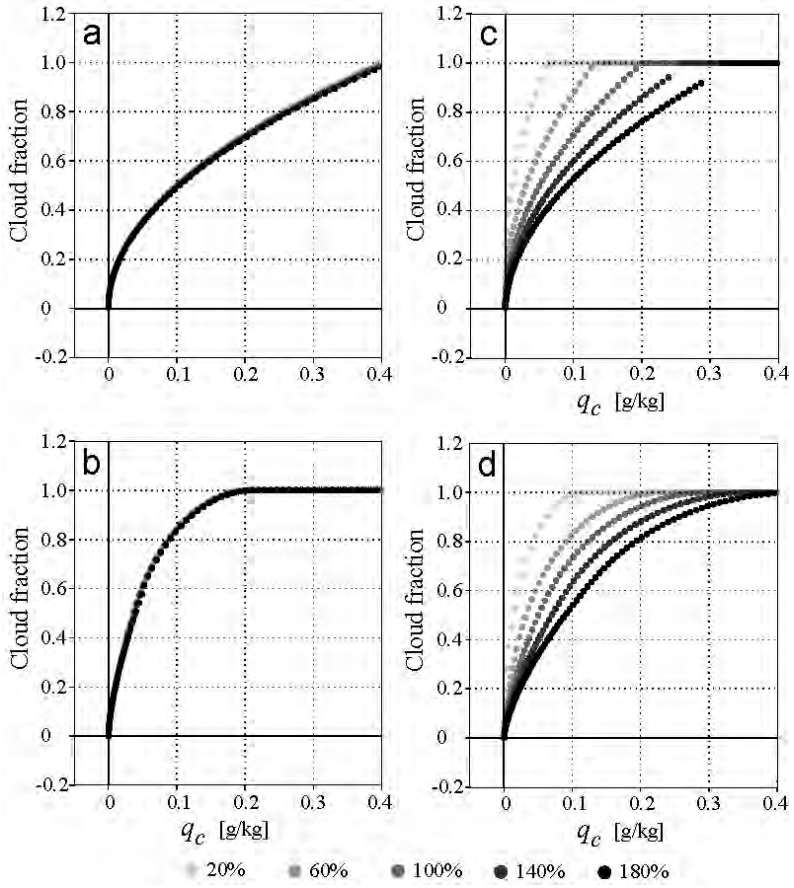

Fig. 2a-d Cloud fraction against cloud water (g kg^{-1}) in the Wilson-Gregory test: **a** LeTreut and Li, **b** Smith, **c** HPC-DU and **d** HPC-ST schemes. The dots with different gray scale indicate the results for different initial cloud water. In **a-b**, the parameters of b=0.1 and RHc=0.9 are used. See text for further details.

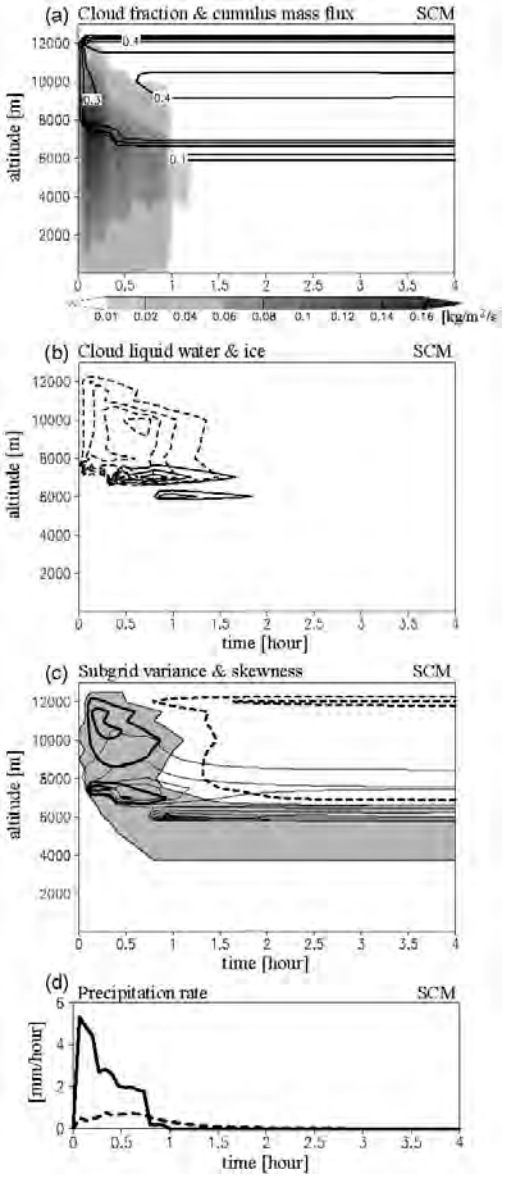

Fig. 3a-d Time evolution in the SCM: **a** cumulus mass-flux (shading) and cloud fraction (contour), **b** cloud liquid water (solid contour) and ice (dashed contour) mixing ratio, **c** PDF variance (thin solid contour) and skewness (thick contour) and **d** convective (solid) and stratiform (dashed) precipitation. The contour interval is 0.02 and 0.05 g kg^{-1} for liquid and ice in **b**, 0.1 g^2 kg^{-2} and 0.5 in **c**. The shaded area in **c** indicates positive skewness.

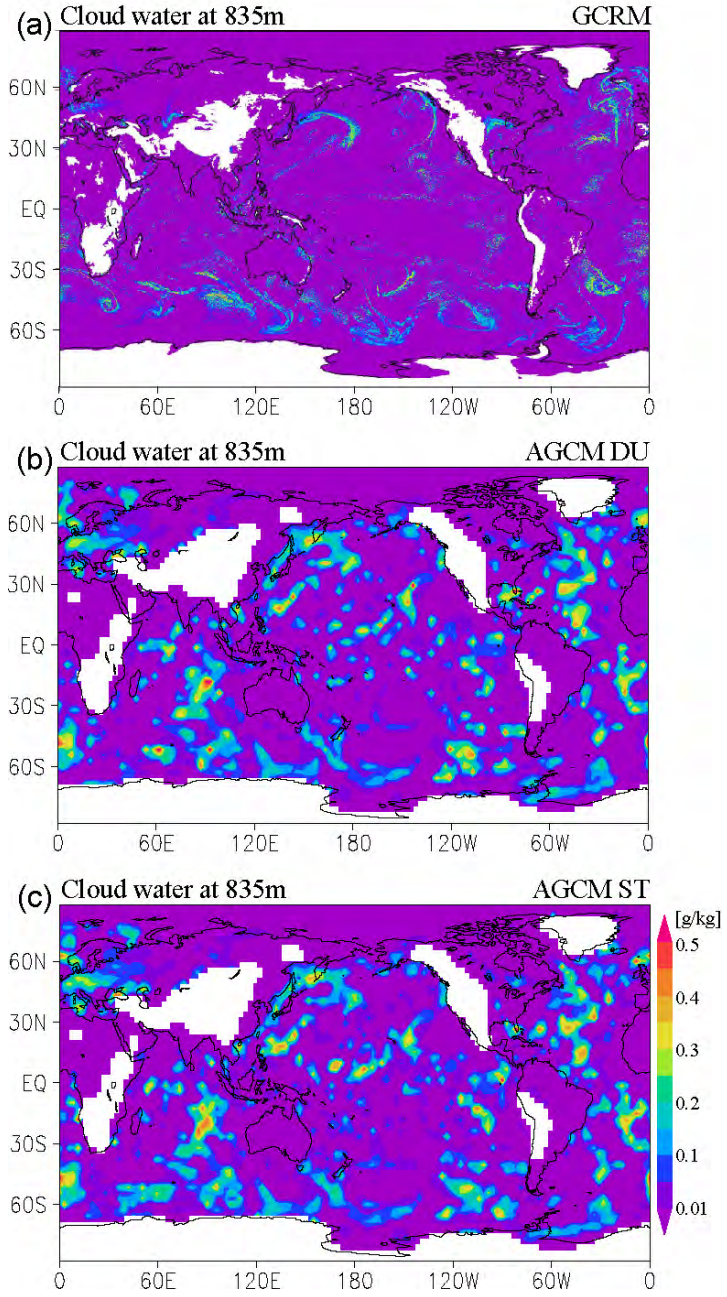

Fig. 4a-d Snapshots of the low-level (z=835 m) cloud water mixing ratio (g kg^{-1}) at 96 h, staring from December 25, 2006: **a** GCRM, **b-c** AGCM with HPC-DU and -ST schemes, respectively.

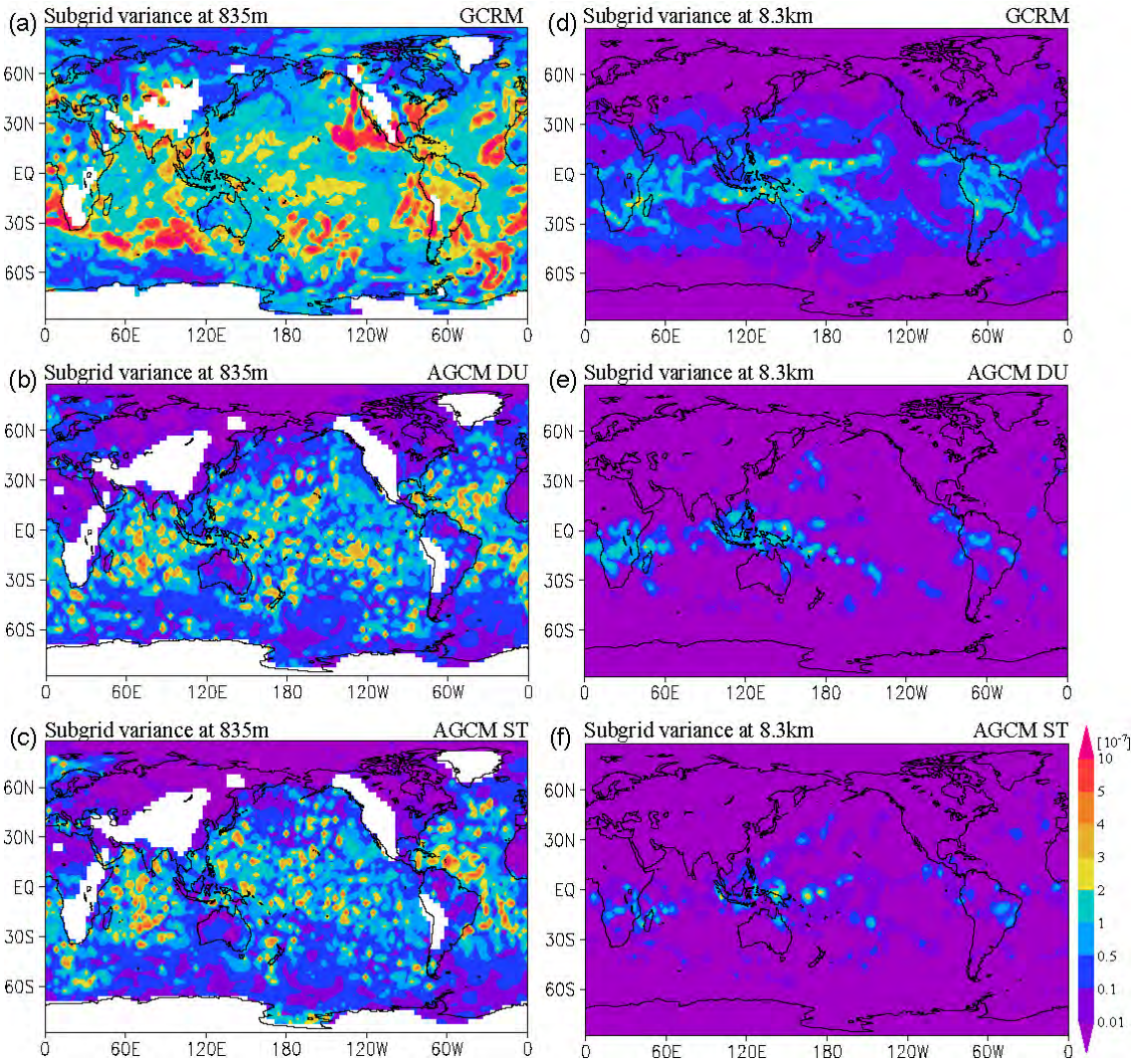

Fig. 5a-f Same as Fig. 4 but for the PDF variance: **a-c** *z*=835 m and **d-f** *z*=8300 m.

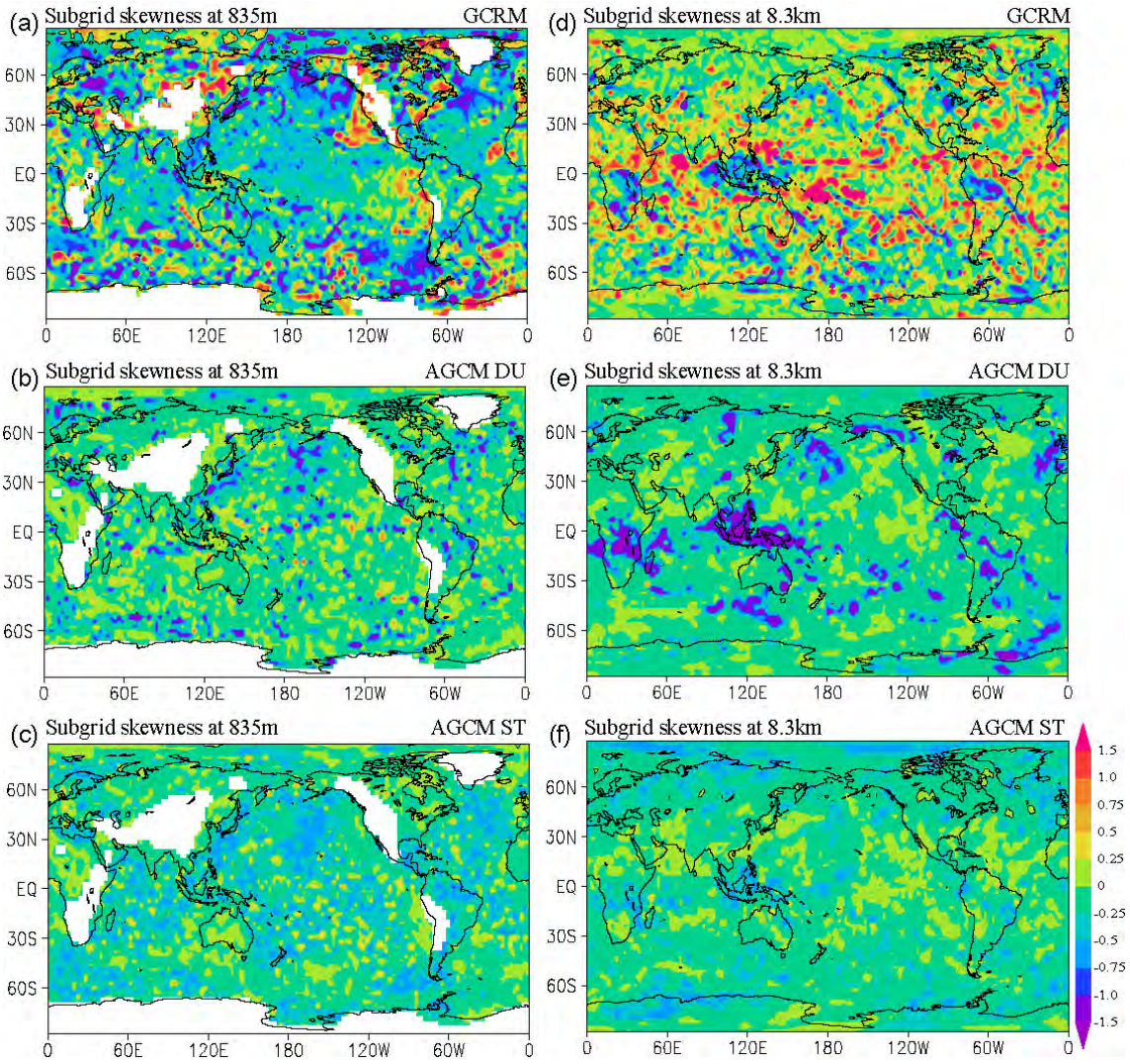

Fig. 6a-f Same as Fig. 4 but for the PDF skewness: **a-c** z=835 m and **d-f** z=8300 m.

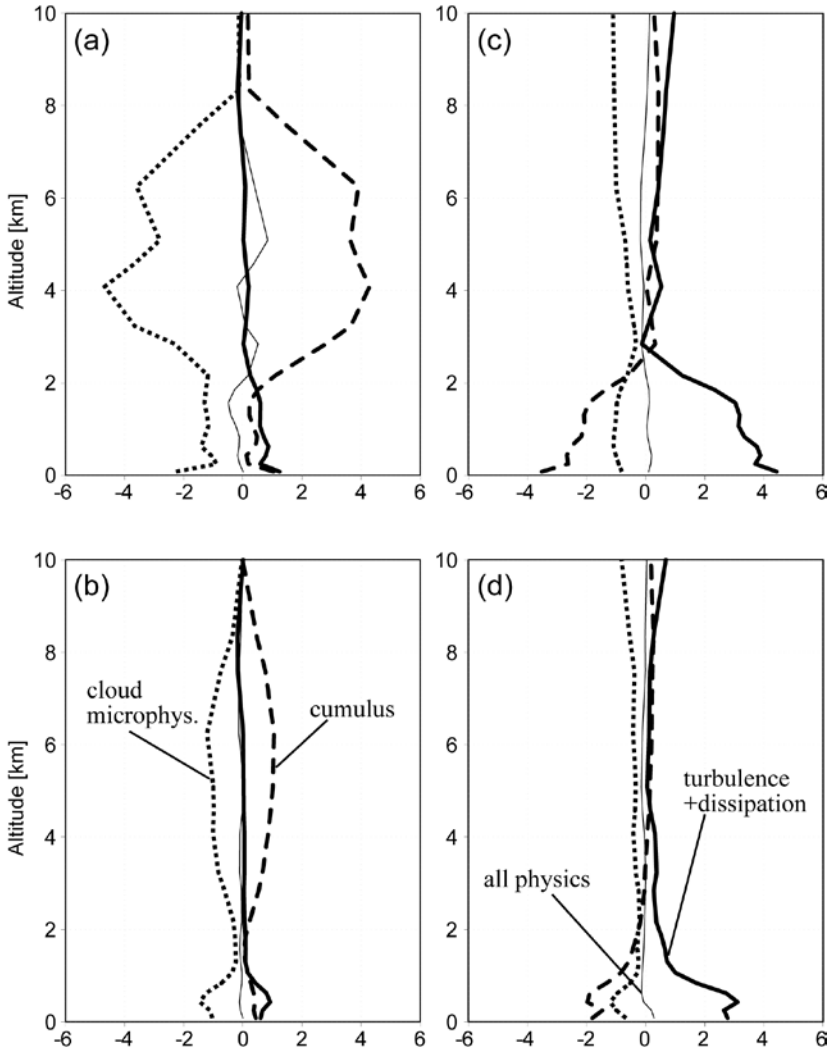

Fig. 7a-d Regionally averaged tendency terms for the PDF variance: **a** western Pacific (100-150E, 20S-20N), **b** eastern off-equatorial Pacific (80-120W, 20S-EQ). The unit is 10^{-6} g^2 kg^{-2} s^{-1} while the dashed, dotted and solid lines denote the tendency due to cumulus, microphysics and turbulence, respectively. **c-d** Same as **a-b** but for the PDF skewness. The unit is 10^{-5} s^{-1}. All the terms are averaged during 72-144 h.

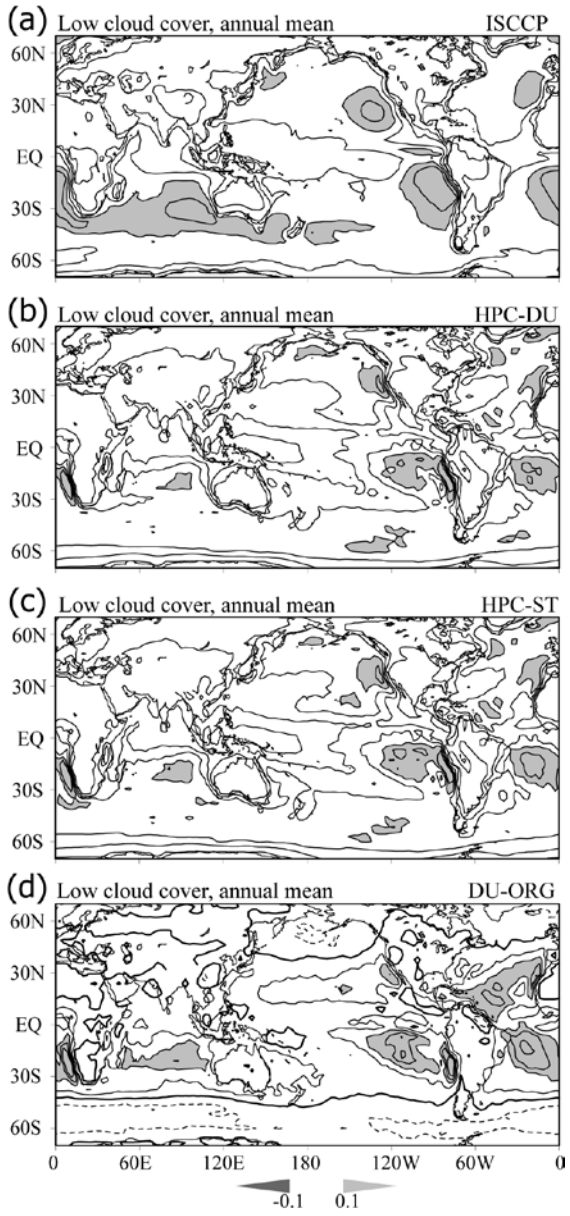

Fig. 8a-c Annual and climatological mean low cloud cover, observed and modeled: **a** ISCCP, **b** HPC-DU, **c** HPC-ST, **d** difference between HPC-DU and the diagnostic scheme (the former minus latter). The contour interval is 0.1 in **a-c** while 0.05 in **d**, negative contours dashed, and light shading denotes values greater than 0.1.

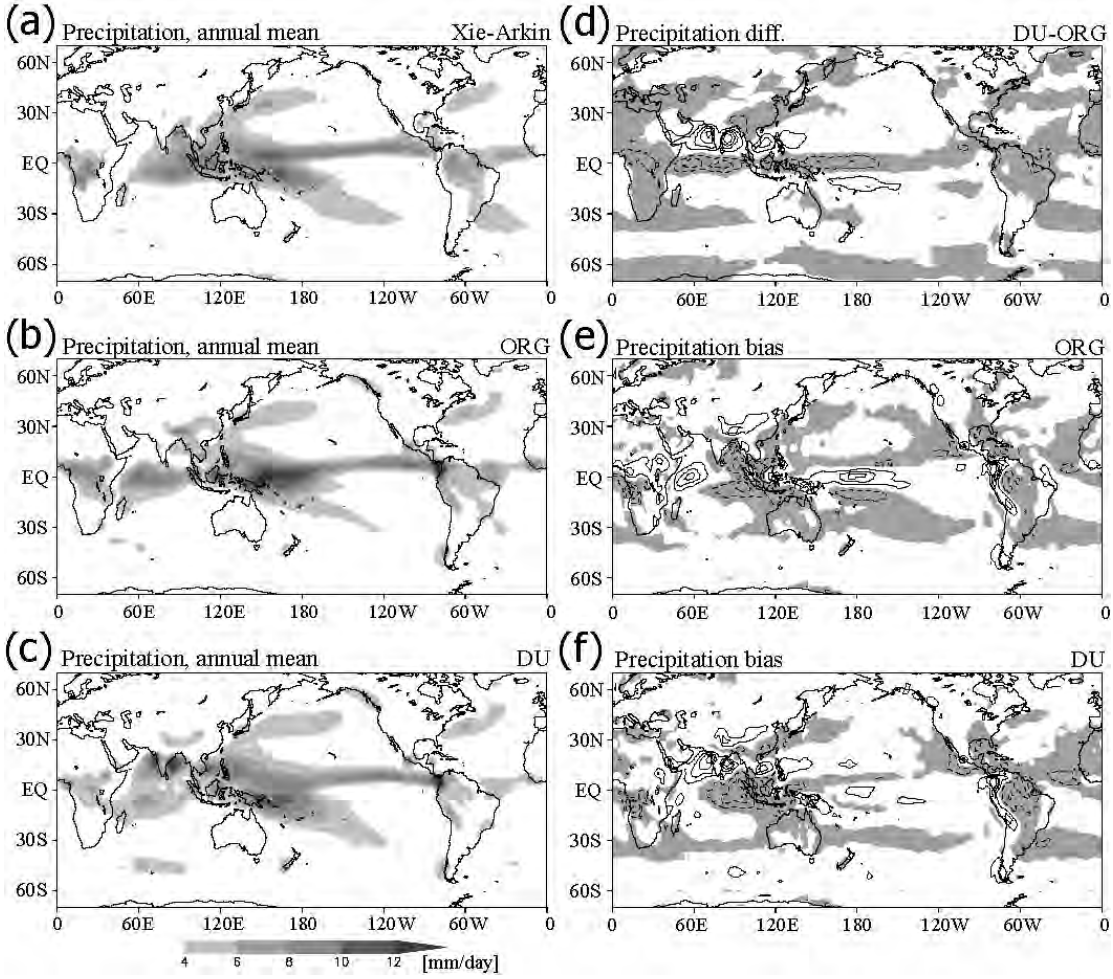

Fig. 9a-f Annual and climatological mean precipitation, observed and modeled: **a** CMAP, **b** diagnostic cloud scheme, **c** HPC-DU, **d** difference between HPC-DU and the diagnostic scheme, **e-f** biases, i.e., differences between **b-c** and **a**. The contour interval is 2 mm day^{-1} in **d-f** while the shading denotes negative values.

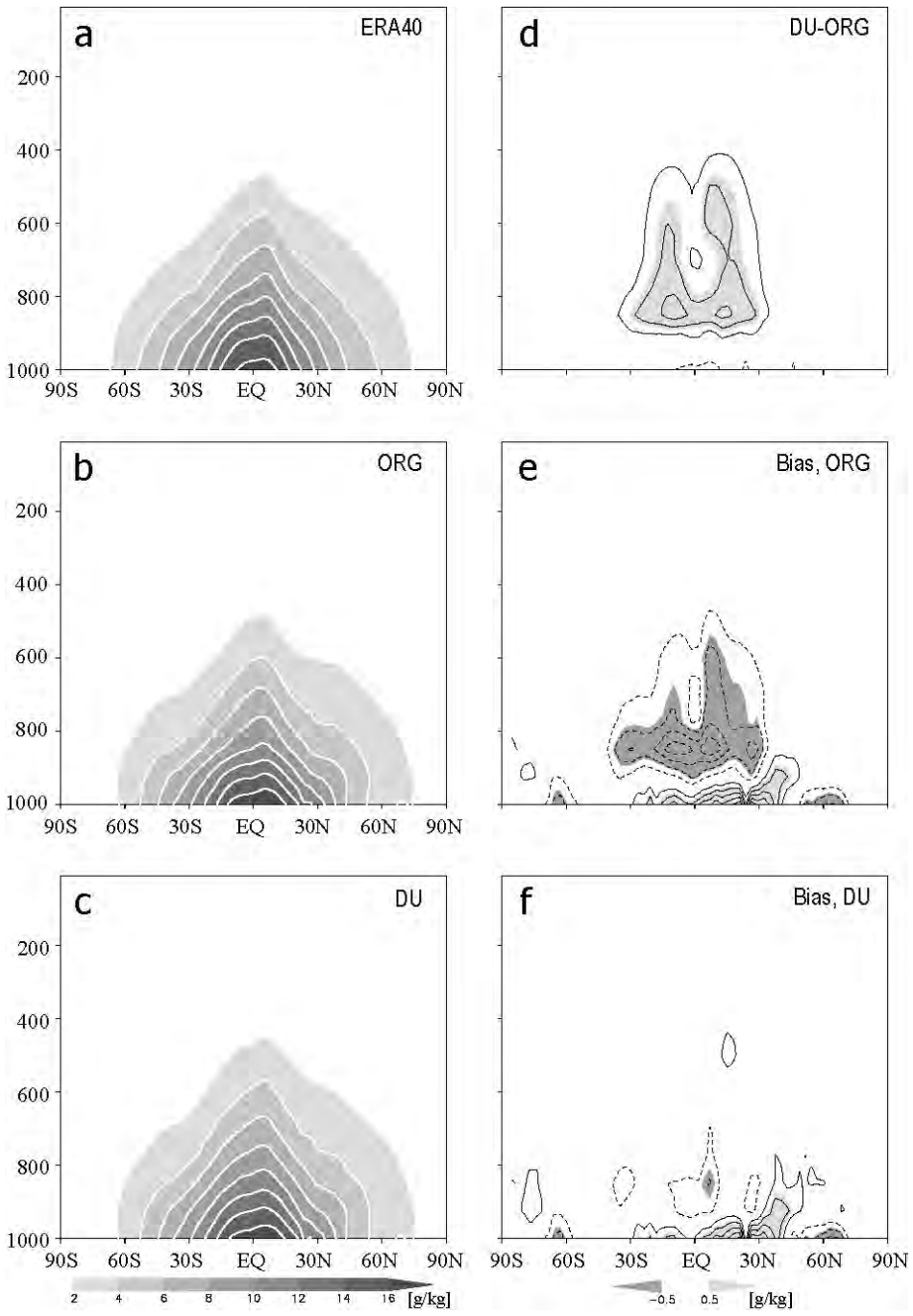

Fig. 10a-f Same as Fig. 9 but for the zonal mean specific humidity. The contour interval in is 2 g kg^{-1} in **a-c** while 0.3 g kg^{-1} in **d-f**. The light (dark) shading in **d-f** denotes the difference or bias greater than 0.5 g kg^{-1} (less than-0.5 g kg^{-1}).

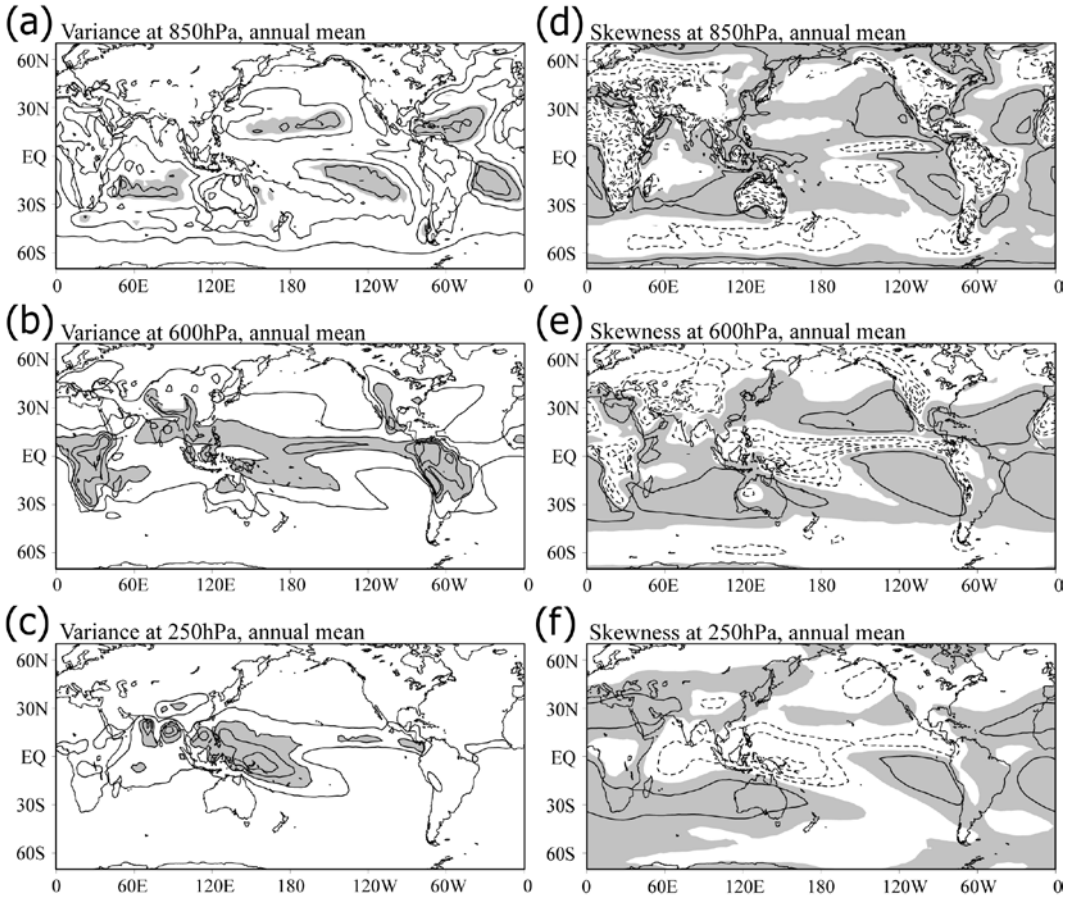

Fig. 11a-f Annual and climatological mean of the PDF moments: **a-c** variance and **d-f** skewness at 850 (upper), 600 (middle), 250 hPa (lower) levels. The contour interval is 3, 1 and 0.1×10^{-2} g^2 kg^{-2} in **a-c** while 0.05 in **d-f**. The shading indicates positive skewness. Note that the horizontal average has been removed in **d-f**.

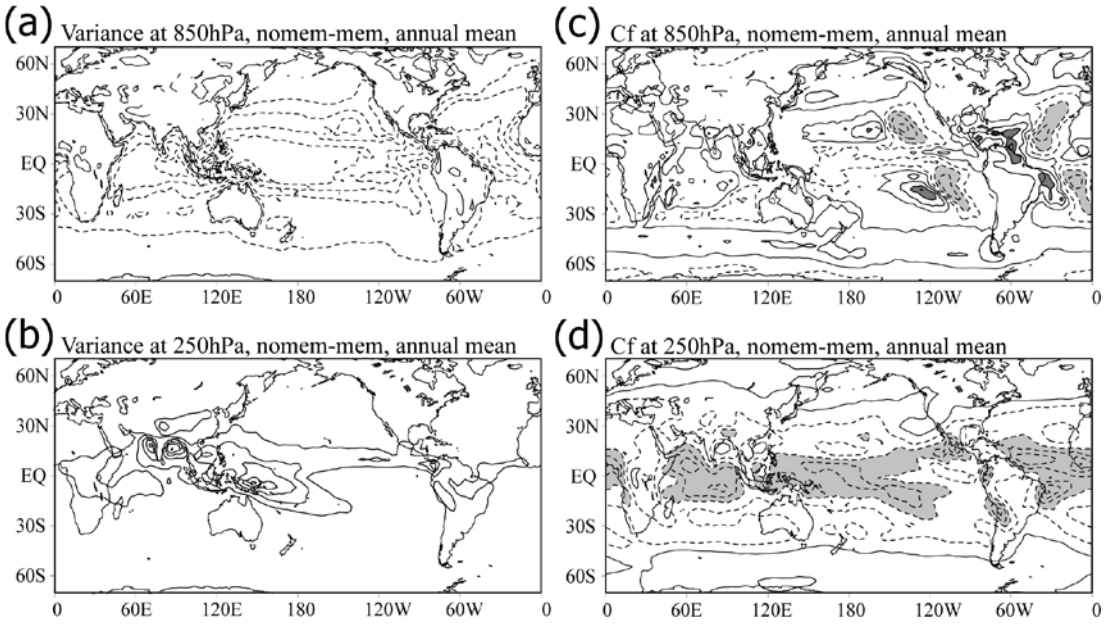

Fig. 12a-d Differences in the annual and climatological mean fields between NOMEM and the control runs (the former minus latter): **a-b** PDF variance at the 850 and 250 hPa levels, **c-d** cloud fraction at the 850 and 250 hPa levels.. The contour interval is 3 and 0.1×10^{-2} g^2 kg^{-2} in **a-b** while 0.05 in **c-d**. The light (dark) shading indicates the difference greater than +0.1 (less than -0.1).

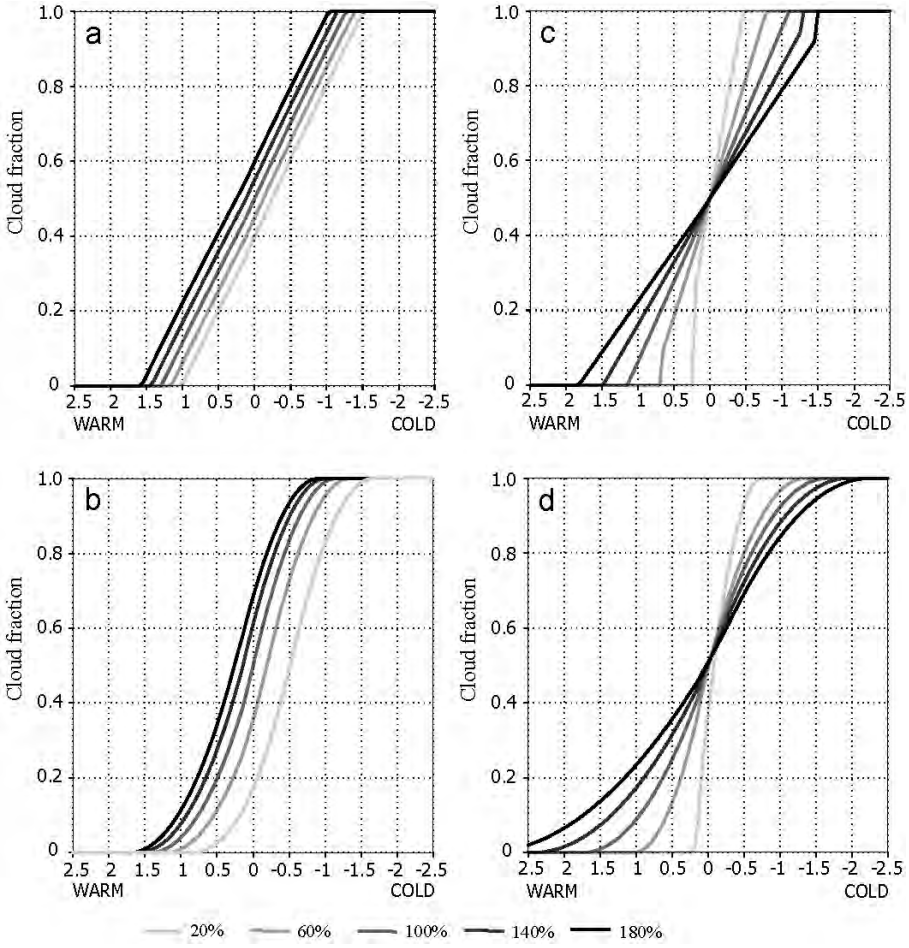

Fig. 13a-d Cloud fraction against temperature change (K) in the Wilson-Gregory test: **a** LeTreut and Li, **b** Smith, **c** HPC-DU and **d** HPC-ST schemes. Lines with different gray scale indicate the results from different initial cloud water. In **a**-**b** parameters of b=0.1 and RHc=0.9 are used. See text for further details.

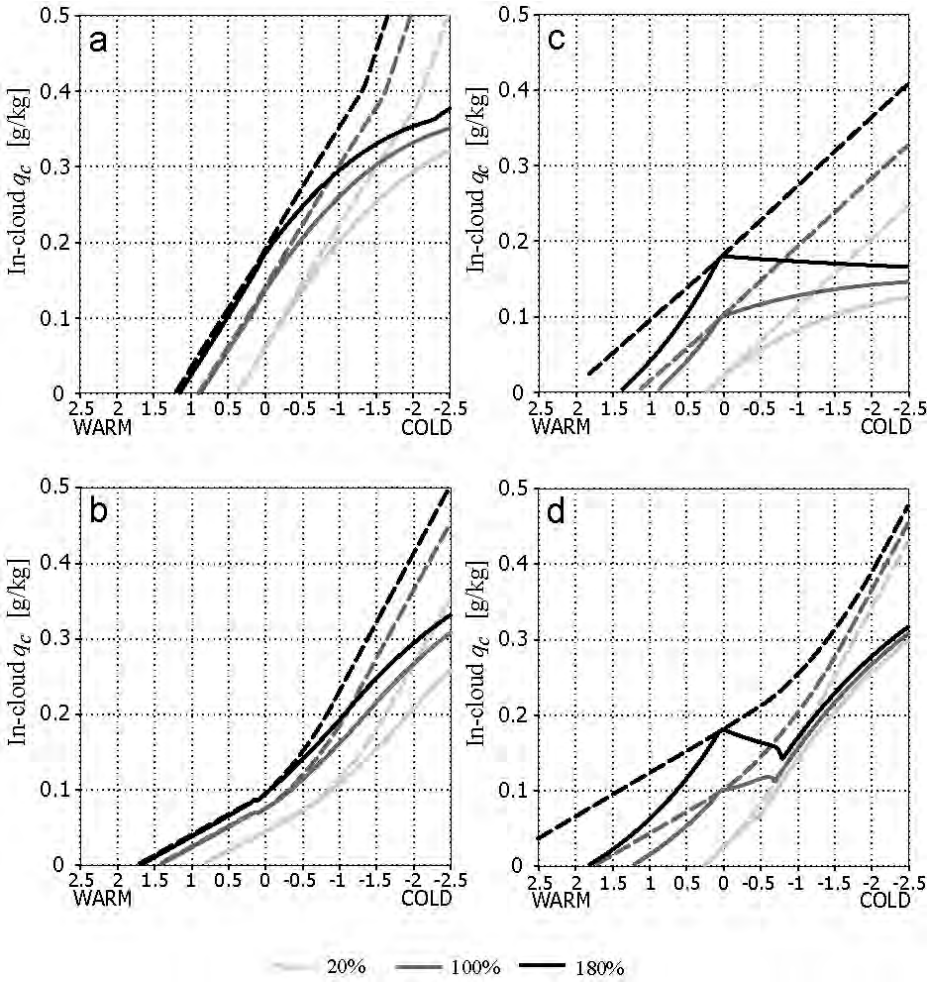

Fig. 14a-d Same as Fig. 13 but for the in-cloud condensate contents (g kg^{-1}). The solid and dashed lines correspond to the results with and without precipitation process, respectively.

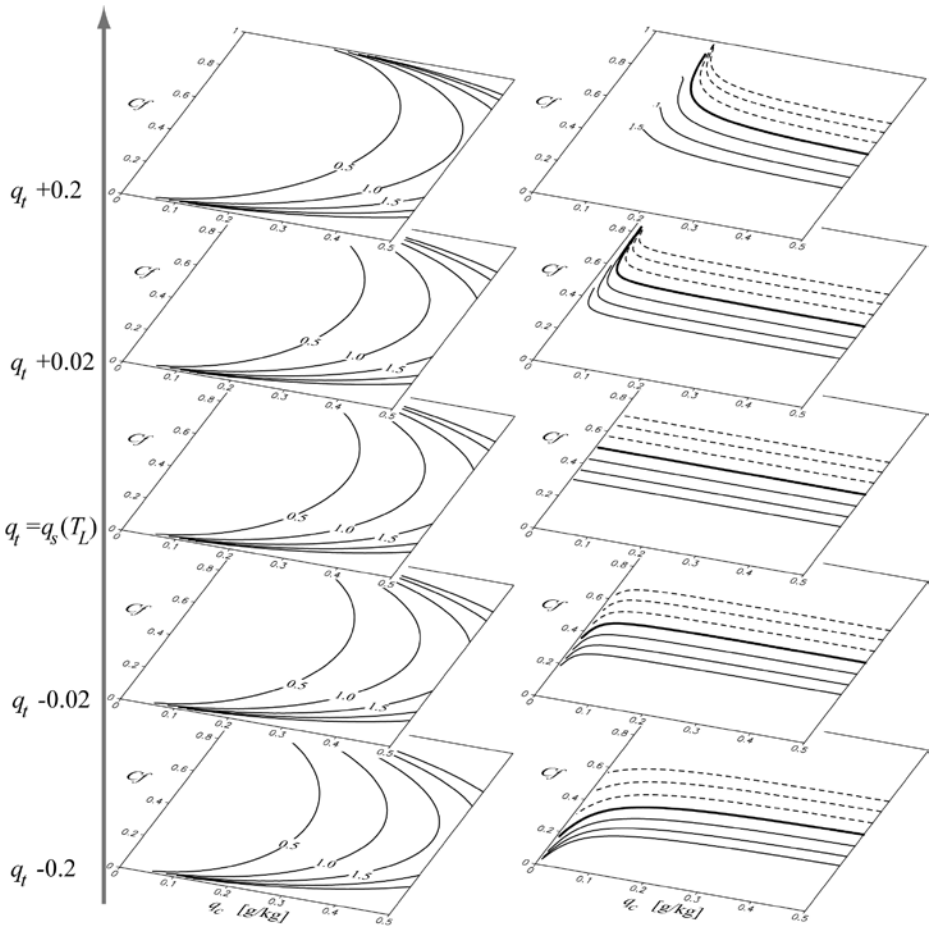

Fig. 15 Dependence of the PDF variance (left) and skewness (right) on the total and cloud water contents and the cloud fraction in the HPC-DU scheme. The contour interval is 0.5 g^2 kg^{-2} for the variance while 0.5 for the skewness. The negative contours are dashed. The other variables are fixed at standard initial values for the Wilson-Gregory test.